Multiscale approach to characterize effective mechanical, hydraulic and acoustic properties of a new bio-based porous material

Q.-B. Nguyen, V.-H. Nguyen, C. Perrot, A. Rios de Anda, E. Renard, S. Naili

Multiscale approach to characterize effective mechanical, hydraulic and acoustic properties of a new bio-based porous material

Q.-B. Nguyen[a,b,c], V.-H. Nguyen[a,b], C. Perrot[d], A. Rios de Anda[c], E. Renard[c], S. Naili[a,b,*]

[a] *Univ Paris Est Creteil, CNRS, MSME, F-94010 Creteil, France*
[b] *Univ Gustave Eiffel, MSME, F-77447 Marne-la-Vallée, France*
[c] *Univ Paris Est Creteil, CNRS, ICMPE, F-94010 Creteil, France*
[d] *MSME, Univ Gustave Eiffel, UPEC, CNRS, F-77454, Marne-la-Vallée, France*

Abstract

This paper is a multi-aspect study which has undertaken essential numerical characterizations of not only mechanical and hydraulic properties but also acoustic behaviour of a new bio-based porous epoxy resin obtained by a "green" adapted combination of the cationic photopolymerization and the porogen leaching technique. This new kind of material generally possesses interconnected fillet-edge cubic pores which lead to more complex morphology than in the case of spherical or cylindrical pores. In order to characterize the effective properties of the material, a multiscale approach using the asymptotic homogenization method has been applied. Such a method has induced cell problems whose the resolutions have been conducted on the geometrical configuration defined from the experimental data of the samples by using Scanning Electron Microscopy (SEM) and Mercury Intrusion Porosimetry (MIP). The sound absorption behaviour of a plate made of the studied material has been subsequently characterized by solving a normal incidence acoustic problem with an assumption of rigid impervious backing. The mechanical model has been validated by balancing numerical results of the sound absorption coefficient, reflection coefficient, surface impedance, equivalent dynamic density and equivalent dynamic bulk modulus with corresponding experimental results obtained by conducting the three-microphone impedance tube testing. As a consequence, the mechanical model has been applied to investigate the influence of microstructural characteristics on effective properties and acoustic performance of the material. To the authors' knowledge, the features of the microstructure obtained from an elaboration process using the porogen leaching technique have rarely been studied in the literature. Four types of ordered pore arrangements together with systematic variations of the porosity and the pore size have been taken under consideration. Based on the results of these investigations, the subtle relation between microstructures and properties has been established. The processing parameters of material elaboration could be adjusted so that the obtained porous material would possess the best sound absorption performance.

Keywords: asymptotic homogenization, effective properties, sound absorption, finite element method, microstructures, bio-based porous epoxy resin, photopolymerization, porogen leaching technique

1. Introduction

Porous materials are used in a large number of industries such as automobile, aeronautic and construction due to their light weight, low production cost and flexible mechanical properties. Most of porous materials have petroleum-based polymeric matrices that come from processes using solvents and amine-type hardeners which are highly toxic to the environment. As an attempt to reduce the consumption of petroleum-based materials, as well as to avoid harmful substances, a novel porous bio-based epoxy resin has been developed by using cationic photopolymerization in conjunction with the porogen leaching technique adapted from [1] and [2]. Unlike the other methods in fabrication of porous materials such as temperature-induced phase separation [3], high internal phase emulsions [4] or gas expansion [5], the porogen leaching technique consists in adding porogen particles to a monomer solution, then in removing the porogen with a corresponding solvent/diluent after the polymerization, thereby obtaining a porous scaffold. This technique includes easy operational steps and permits accurate control of pore size and porosity [6, 7]. It is also relevant to the cationic photopolymerization because this kind of polymerization is relatively solvent-sensitive. Therefore, the presence of a solvent during the polymerization step is not required [8].

The determination of the effective mechanical, hydraulic and acoustic characteristics of these materials is essential, in particular, during the elaboration phase of the material. In order to characterize the effective properties of these materials, experimental methods could be used to determine, for instance: (i) the effective elastic modulus *via* uniaxial compression tests; (ii) the effective static permeability *via* the application of Darcy's law under steady state conditions; (iii) acoustic properties *via* impedance tube experiments associated with the transfer function (or transfer matrix methods). Most of these methods require specific facilities and huge effort in conducting experiments that are usually related to complicated characterization techniques. Particularly, it remains challenging for measurements of frequency-dependent properties such as dynamic permeability or dynamic compressibility. In addition, only a few methods establish a useful relation between material microstructures and effective properties.

Among the methods for modelling porous materials, the average-field theory and the asymptotic homogenization are the most convenient and commonly accepted ones, since they enable the estimation of all mechanical properties of a poroelastic medium. One of the major differences between them is the choice of the representative volume element (RVE), or a "representative cell" for performing calculations related to each of these techniques: while the RVE of a statistically homogeneous body is employed in the average-field theory, the asymptotic homogenization theory is based on the representative (unit) periodic cell. The

*Corresponding author
Email address: naili@u-pec.fr (S. Naili)

homogenization theory starts at the microscopic scale with the detailed microstructure of the pores, the linearized equations of elasticity and the linearized equations of fluid dynamics (see for instance [9] for a mechanical point of view and [10] for a mathematical point of view). As a consequence, the effective properties in the conservation equations (continuity and momentum equations) and in the constitutive relations at the macroscopic scale are obtained according to the geometrical and mechanical properties of the microstructure. This multiscale approach based on the asymptotic homogenization theory has been used with success in several recent papers to characterize new materials [11, 12].

It is well-known that the effective properties and acoustic performance of porous materials strongly depend on the mechanical properties of the solid phase, the pore size, the porosity and the pore arrangement. Published research works in the open literature have mainly focused on the microstructures with idealized geometries such as spherical, cylindrical, cross-type or sometimes polyhedral pores [13, 14]. To the best of our knowledge, few studies have been carried out on the influence of microstructural parameters related to the case of fillet-edge cubic pores which mimic the pores of the above-mentioned novel porous bio-based material and result in more complex morphology than the ones cited above. Furthermore, these studies focused on only either effective mechanical properties or acoustic characteristics of materials and none of them simultaneously investigated both aspects.

The main objective of this study is to perform numerical characterizations of effective mechanical, hydraulic and acoustic properties of the novel bio-inspired porous epoxy resin, which is synthesized through a relevant combination of the cationic photopolymerization and the porogen leaching technique. The obtained results may allow us to make essential suggestions for improving the elaborated material. Although the above-mentioned works are related to the same topic, the present paper contributes to the modelling of the porous media in several aspects. Indeed, the paper supplies original understandings of the influence of the microstructural features, namely the pore arrangement, the porosity, and finally, the pore size on the effective properties and acoustic performance of the porous material possessing interconnected pores with the specific fillet-edge cubic shape. To the authors' knowledge, the features of this microstructure which is obtained from an elaboration process using the porogen leaching technique have been rarely studied in the literature. By considering simultaneously the effective mechanical properties, the effective permeability and compressibility as well as the acoustic behaviour of the material, this multi-aspect study provides a relevant insight into the microstructures-properties relation, creating the foundations of a potential development for studied porous epoxy resins in a wide range of applications.

In order to characterize the elaborated porous material, a multiscale approach based on the asymptotic homogenization has been used. The resolution of the asymptotic homogenization problems, called the cell problems, has been carried out by considering idealized cell structures obtained from the imaging of sample microstructures which allows to determine, in particular, the geometrical properties of microstructures. Using homogenization results, the sound absorption problem of a porous plate made of the studied material has been studied. The validation of the mechanical model has been confirmed by comparing the numerical results of the effective acoustic properties and the measurements obtained from the three-microphone impedance tube testing. The multiscale approach has been then

used to investigate the effect of microstructural characteristics on the effective properties and the acoustic behaviour of the material. For this purpose, four different ordered pore arrangements as well as systematic variations of the porosity and the pore size have been taken into account.

The paper is organized as follows. The elaboration and experimental pore characterization of the porous material is introduced in Section 2. We present in Section 3 the principles and main formulations of the asymptotic homogenization procedure. The construction of idealized representative volume elements is presented in Section 4. The description of the normal incidence sound absorption problem in case of a structural poroelastic plate is provided in Section 5. The numerical results and a discussion are proposed in the Section 6. In this section, an experimental validation of the mechanical model, as well as the influence of microstructural characteristics on the effective properties and sound absorption performance of the material are discussed. Section 7 completes the paper with main conclusions.

2. Material elaboration and characterization

2.1. Elaboration process using porogen leaching technique

The porous polymeric material was elaborated using the cationic photopolymerization in conjunction with the porogen leaching technique, which involved the presence of chloride sodium (NaCl) templates. The key idea of introducing NaCl particles in the process is that the removal of these particles after the polymerization will leave the empty space, creating porosity in the material (see Fig. 1). NaCl templates with a cylindrical shape of circular cross-section, whose the diameter and height are respectively equal to 5.1 cm and 0.5 cm, were produced by the Spark Plasma Sintering (SPS) technique using NaCl cubic particles whose the size varied between 250 and 400 μm. This sintering technique induces simultaneously a variation of heat and pressure on NaCl particles, carrying out the contacts among NaCl particles, thereby ensuring the pore interconnection of the obtained porous material [15]. From NaCl mass and the dimensions of the templates, the NaCl volume fraction is about 82%.

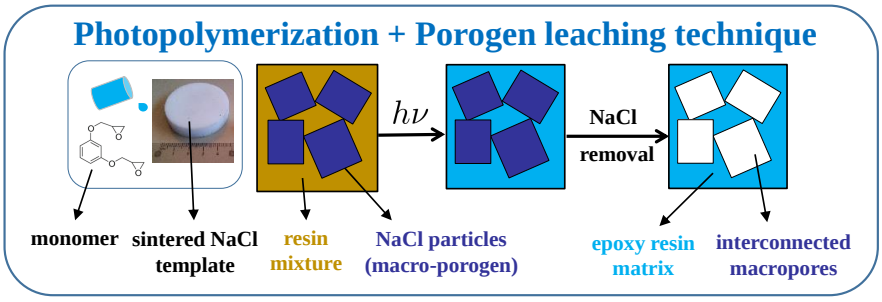

Figure 1: Schema of porogen leaching technique using NaCl particles as macro-porogen.

The resin was composed of resorcinol diglycidyl ether as monomer, bis (dodecylphenyl) iodonium hexafluoro-antimonate (herein called Iod) as photoinitiator and benzophenone as photosensitizer. The masses of Iod and benzophenone were 5% and 1% of the monomer mass,

respectively. After being melted at a temperature of 120°C, the liquid-state resin mixture was introduced into the NaCl template which was isolated under vacuum beforehand. According to our rheological study, the considered mixture reaches its lowest dynamic viscosity at a temperature greater than or equal to 120°C. The combination of melting the resin mixture at this temperature and the vacuum-state of the template helps the mixture deeply penetrate into the template and fill up the space between NaCl particles. The new mixture (resin mixture - NaCl template) was then isolated under vacuum for 30 min to ensure the resin's penetration. After that, this new mixture was irradiated by a polychromatic spot with a UV wavelength from 250 to 450 nm and an intensity of 220 W/m^2. The irradiation was carried out on each circular face of the template for 30 min. Subsequently, the new mixture was placed in an oven at 120°C for 1.5 h to finish the polymerization. Finally, NaCl particles were removed by immersing this mixture in water for 72 h. The water was changed every 12 h. The wet sample was then placed under vacuum for 24 h to obtain the final dry porous sample. The complete NaCl removal was verified by the gravimetric method. Note that the interconnected porous network after the removal of sintered NaCl particles has been confirmed by SEM images. Besides, the fusion of NaCl cubic particles has many contact/fusion modes, for intance, "face to face", "side to side" and "point to point" modes, but the "face to face" mode has been more frequently found in SEM micrographs. This contact mode has resulted in the large entrance towards a pore as determined by MIP measurements.

With the proposed technique, the porosity can be adjusted to obtain materials with larger or smaller porosities. Indeed, the porosity of the resulting material can easily be altered by adjusting the pressure and the temperature during template preparation by the SPS process. Raising the pressure and the temperature during the SPS process induces a sintered porogen template with more porogen constituents in a volume, which means a final material with more porosity. On the contrary, the process with lower pressure and lower temperature leads to a material with a smaller porosity.

2.2. Experimental pore characterization

Pore features of the obtained porous material was then characterized by Mercury Intrusion Porosimetry (MIP) and Scanning Electron Microscopy (SEM). According to MIP results, the distribution of pore size is centered at about 180 μm. This value is smaller than the size of NaCl particles used in the fabrication of templates (*i.e.*, 250-400 μm) due to the fact that during the tests by MIP, at each level of mercury pressure, one measures the largest entrance towards a pore, but not the actual inner size of a pore [16]. The dimension of this entrance is smaller than the inner pore size which is similar to particle size. The analysis of SEM micrographs (see Fig. 2) gives the average value of entrance dimension which is about 192 μm, showing a good agreement with the profile obtained by the MIP.

The tests of MIP also provided a porosity value of about 43%. It is noted that this value is much smaller than the NaCl volume fraction of 82%, which would be the value of porosity in case of perfect penetration of the resin mixture into the template. This is explained by the fact that the use of NaCl particles, whose the size varies between 250 and 400 μm, lead to the existence of pore sizes that were beyond the pore size range (0.003-360 μm) that

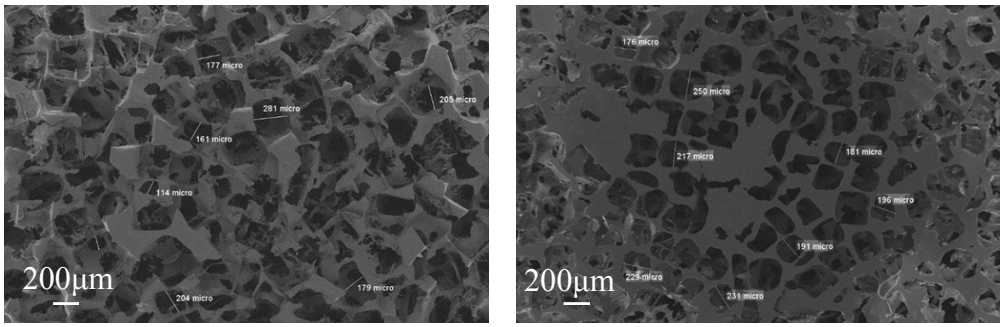

Figure 2: SEM micrographs: (left) on cross-section; (right) on external surface

the experimental setup can afford. The porosity was also determined by another approach. By taking a piece of the porous material, weighing and measuring its dimensions to obtain its mass m and volume V, the volumetric density of the porous material is determined as $\rho = m/V$. Based on the density of the matrix phase ρ^s which was identified when working with the bulk material, we can find the porosity by the relation $\phi = 1 - \rho/\rho^s$. This approach gave a porosity of approximately 83% which correlates with the NaCl volume fraction. The fact that this value is slightly greater than the NaCl volume fraction is explained by considering that the resin mixture did not perfectly penetrate and did not fill in all of the spaces among NaCl particles. Therefore, the value of 83% was considered as the porosity of the obtained porous material.

3. Homogenization and effective properties

In what follows, the Cartesian reference system is used in which the orthonormal basis is denoted by $(\mathbf{e}_1, \mathbf{e}_2, \mathbf{e}_3)$. The coordinates of a point are specified by (x_1, x_2, x_3). The time coordinate is denoted by t. The time derivative is denoted by a superimposed dot. Einstein's summation convention about the repeated indices is used. The imaginary pure number denoted by i is defined by $\mathrm{i}^2 = -1$. All fields are written in the frequency domain, considering a harmonic regime with functions proportional to $\exp(\mathrm{i}\omega t)$ where ω is the angular frequency.

3.1. Two-scale asymptotic homogenization procedure

The details of the two-scale asymptotic homogenization procedure, the derivation of cell problems and macroscopic state equations can be found, for instance, in [17] and [18]. The following parts present the principle and the main results obtained by this method.

We consider a deformable porous medium saturated by a fluid. It is assumed that the constitutive relations are the one of a linearly elastic solid for the skeleton and the one of a Newtonian compressible fluid whose dynamic viscosity is η for the fluid phase. The domain of a representative volume element is denoted by $Y \subset \mathbb{R}^3$ at the microscopic scale and is decomposed into the matrix (the skeleton which composes the solid phase) and the pore subdomains. These subdomains are respectively denoted by Y^s and Y^f, and their common

boundary is designated by Γ^{sf} (see Fig. 3):

$$Y = Y^s \cup Y^f \cup \Gamma^{sf}, \qquad Y^s \cap Y^f = \emptyset, \qquad \Gamma^{sf} = \partial Y^s \cap \partial Y^f. \tag{1}$$

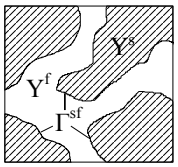

Figure 3: Sketch of the studied microscopic domains.

The pores of the medium are assumed to be interconnected throughout the whole domain.

3.1.1. Microscopic governing equations

In the solid phase, the momentum and constitutive equations read:

$$\frac{\partial \sigma_{ij}^s}{\partial x_j} = -\rho^s \omega^2 u_i^s \qquad \text{within } Y^s, \tag{2a}$$

$$\sigma_{ij}^s = c_{ijkl}^s \varepsilon_{kl}^s, \tag{2b}$$

where ρ^s, u_i^s and σ_{ij}^s are respectively the density, the components of the displacement vector and stress tensor. The quantities c_{ijkl}^s are the components of the fourth-order elasticity tensor. The components ε_{kl}^s are the components of the infinitesimal strain which read:

$$\varepsilon_{kl}^s = \frac{1}{2}\left(\frac{\partial u_k^s}{\partial x_l} + \frac{\partial u_l^s}{\partial x_k}\right) \tag{3}$$

In the fluid phase, the governing equations are the law of mass conservation and the state equation of gas:

$$\rho^f \frac{\partial v_i^f}{\partial x_i} + \mathrm{i}\omega\delta^f = 0 \qquad \text{within } Y^f, \tag{4a}$$

$$\frac{\delta^f}{\rho^f} + \frac{\tau^f}{T^f} = \frac{p^f}{P^f} \qquad \text{within } Y^f, \tag{4b}$$

where p^f and v_i^f are respectively the pressure and the components of the velocity of the fluid phase; P^f, ρ^f and T^f are respectively the pressure, the density and the temperature of the fluid phase in the rest state; δ^f and τ^f are respectively the perturbations of the density and the temperature.

Due to the fact that infinitesimal harmonic motions are supposed to be in the fluid phase, the Navier-Stokes equation for the compressible viscous fluid can be linearized and written as:

$$\frac{\partial \sigma_{ij}^f}{\partial x_j} = \rho^f \mathrm{i}\omega v_i^f \qquad \text{within } Y^f, \tag{5}$$

where the constitutive equation of compressible viscous fluid and the infinitesimal strain rate are given by:

$$\sigma_{ij}^f = 2\eta\dot{\varepsilon}_{ij}^f - \frac{2}{3}\eta\dot{\varepsilon}_{kk}^f\delta_{ij} - p^f\delta_{ij}, \tag{6a}$$

$$\dot{\varepsilon}_{ij}^f = \frac{1}{2}\left(\frac{\partial v_i^f}{\partial x_j} + \frac{\partial v_j^f}{\partial x_i}\right), \tag{6b}$$

where δ_{ij} is the Kronecker symbol.

As regards the thermal field, the solid phase can maintain isothermal conditions when the specific heat capacity of the solid phase is much larger than that of the fluid phase. By denoting q_i^f and κ_{ij}^f respectively the components of the thermal flux and thermal conductivity from the energy conservation law associated with the specific heat under constant volume and the universal gas constant denoted respectively by C_v^f and R_g, the set of governing equations for the thermal field in the fluid phase is expressed as:

$$-\frac{\partial q_i^f}{\partial x_i} = \mathrm{i}\omega\rho^f C_V^f\tau^f + \left(\mathrm{i}\omega\rho^f R_g\tau^f - \mathrm{i}\omega\rho^f\right) \qquad \text{within } Y^f, \tag{7a}$$

$$q_i^f = -\kappa_{ij}^f\frac{\partial\tau^f}{\partial x_j} \qquad \text{within } Y^f. \tag{7b}$$

For an ideal gas, Mayer's relation is valid and is given by the relation $C_P^f - C_V^f = R_g$, where C_P^f is the specific heat under constant pressure. It is also convenient to introduce the specific heat ratio of the fluid $\gamma^f = C_P^f/C_V^f$ which will be used in the next sections.

The continuity conditions at the common boundary Γ^{sf} of the solid and fluid phases for the normal stress, the velocity and the temperature are given as follows:

$$\sigma_{ij}^s n_j^s + \sigma_{ij}^f n_j^f = 0 \qquad \text{over } \Gamma^{sf}, \tag{8a}$$

$$\mathrm{i}\omega u_i^s = v_i^f \qquad \text{over } \Gamma^{sf}, \tag{8b}$$

$$\tau^f = 0 \qquad \text{over } \Gamma^{sf}, \tag{8c}$$

where n_j^s and n_j^f are the components of outward normal unit vectors to the boundary Γ^{sf}, corresponding to the solid and fluid phases, respectively.

3.1.2. Scaling and asymptotic expansions

A poroelastic medium that has a geometrically periodic microstructure is considered. The unit length of the periodicity is denoted by l and the macroscopic characteristic length by L. It is assumed that the scale ratio $\epsilon = l/L$ is much smaller than 1, that is, the two scales l and L differ significantly from each other. The position vector at the macroscopic scale is denoted by $\boldsymbol{x}$ (whose components are given by x_i), and the position vector at the microscopic scale by $\boldsymbol{y} = \boldsymbol{x}/\epsilon$ (the components are $y_i = x_i/\epsilon$).

Sound absorption is generally attributed to viscous damping and thermal dissipation which occur in the vicinity of the solid-fluid interface. Furthermore, in the air, the heat conductivity is isotropic and is defined by a tensor whose components are $\kappa_{ij}^f = \kappa_0^f \delta_{ij}$ where κ_0^f is the characteristic thermal conductivity of the air. So, the thicknesses of the region where these energy exchanges take place are respectively called the viscous skin depth $\delta_v = (2\eta/(\rho^f\omega))^{1/2}$ and the thermal skin depth $\delta_t = (\kappa_0^f/(\rho^f\omega C_P^f))^{1/2}$. When a poroelastic material that is saturated with the air is capable of absorbing sounds, both thicknesses are on the same order as that of the pore scale [18], leading to the relation $O(\delta_{v,t}^2/L^2) = O(\epsilon^2)$ where $O(*)$ is big-oh notation, which is used to describe the asymptotic behaviour of the function. Consequently, equations (6) and (7b) can respectively be rewritten as:

$$\sigma_{ij}^f = 2\epsilon^2\eta\dot{\varepsilon}_{ij}^f - \frac{2}{3}\epsilon^2\eta\dot{\varepsilon}_{kk}^f\delta_{ij} - p^f\delta_{ij}, \tag{9}$$

$$q_i^f = -\epsilon^2\kappa_{ij}^f\frac{\partial\tau^f}{\partial x_j}. \tag{10}$$

We assume a solution in the asymptotically expanded form for physical variables u_i^s, v_i^f, p^f, τ^f and δ^f [19]:

$$\begin{aligned}
u_i^s &= u_i^{s(0)}(\boldsymbol{x},\boldsymbol{y}) + \epsilon u_i^{s(1)}(\boldsymbol{x},\boldsymbol{y}) + \epsilon^2 u_i^{s(2)}(\boldsymbol{x},\boldsymbol{y}) + \dots,\\
v_i^f &= v_i^{f(0)}(\boldsymbol{x},\boldsymbol{y}) + \epsilon v_i^{f(1)}(\boldsymbol{x},\boldsymbol{y}) + \epsilon^2 v_i^{f(2)}(\boldsymbol{x},\boldsymbol{y}) + \dots,\\
p^f &= p^{f(0)}(\boldsymbol{x},\boldsymbol{y}) + \epsilon p^{f(1)}(\boldsymbol{x},\boldsymbol{y}) + \epsilon^2 p^{f(2)}(\boldsymbol{x},\boldsymbol{y}) + \dots,\\
\tau^f &= \tau^{f(0)}(\boldsymbol{x},\boldsymbol{y}) + \epsilon\tau^{f(1)}(\boldsymbol{x},\boldsymbol{y}) + \epsilon^2\tau^{f(2)}(\boldsymbol{x},\boldsymbol{y}) + \dots,\\
\delta^f &= \delta^{f(0)}(\boldsymbol{x},\boldsymbol{y}) + \epsilon\delta^{f(1)}(\boldsymbol{x},\boldsymbol{y}) + \epsilon^2\delta^{f(2)}(\boldsymbol{x},\boldsymbol{y}) + \dots,
\end{aligned} \tag{11}$$

where all the functions on the right-hand side of Eqs.(11) are Y-periodic, *i.e.*, periodic in terms of $\boldsymbol{y}$ with the period of a representative volume element Y, and the superscripts (n) represent explicitly the terms of the order of ϵ^n. All of these expansions are then substituted into Eqs. (2)-(10).

3.1.3. Cell problems

By plugging the asymptotic expansions of Eq. (11) in Eqs.(2)-(10), one can deduce four cell problems which will be used for the determination of effective properties of the poroelastic medium. By introducing the functional spaces $\mathcal{C}_{\#}(Y^{s,f})$ of Y-periodic functions which are sufficiently differential on $Y^{s,f}$, cell problems can be written in their weak forms as follows:

Cell problem 1: Find the function $\chi_p^{kl}(\boldsymbol{y}) \in \mathcal{C}_{\#}(Y^s)$ such as:

$$\int_{Y^s}\Big(c_{ijkl}^s - c_{ijpq}^s\frac{\partial\chi_p^{kl}(\boldsymbol{y})}{\partial y_q}\Big)\frac{\partial\delta\chi_i^{kl}(\boldsymbol{y})}{\partial y_j}\mathrm{d}V = 0, \qquad \forall\delta\chi_i^{kl}(\boldsymbol{y}) \in \mathcal{C}_{\#}(Y^s), \tag{12a}$$

$$\int_{Y^s}\chi_p^{kl}(\boldsymbol{y})\mathrm{d}V = 0. \tag{12b}$$

Cell problem 2: Find $\beta_k(\boldsymbol{y}) \in \mathcal{C}_{\#}(Y^s)$ such as:

$$\int_{Y^s} c^s_{ijkl} \frac{\partial \beta_k(\boldsymbol{y})}{\partial y_l} \frac{\partial \delta\beta_i(\boldsymbol{y})}{\partial y_j} \mathrm{d}V = \int_{\Gamma^{sf}} \delta_{ij} n^s_j \delta\beta_i(\boldsymbol{y}) \mathrm{d}\Gamma, \qquad \forall \delta\beta_i(\boldsymbol{y}) \in \mathcal{C}_{\#}(Y^s), \tag{13a}$$

$$\int_{Y^s} \beta_k(\boldsymbol{y}) \mathrm{d}V = 0. \tag{13b}$$

Cell problem 3: Find the functions $\xi^k_i(\boldsymbol{y})$ and $\pi^k(\boldsymbol{y}) \in \mathcal{C}_{\#}(Y^f)$ such as:

$$\int_{Y^f} \rho^f \mathrm{i}\omega \xi^k_i(\boldsymbol{y}) \delta\xi^k_i(\boldsymbol{y}) \mathrm{d}V + \int_{Y^f} \eta \frac{\partial \xi^k_i(\boldsymbol{y})}{\partial y_j} \frac{\partial \delta\xi^k_i(\boldsymbol{y})}{\partial y_j} \mathrm{d}V$$
$$- \int_{Y^f} \frac{\partial \delta\xi^k_i(\boldsymbol{y})}{\partial y_i} \pi^k(\boldsymbol{y}) \mathrm{d}V = \int_{Y^f} \delta\xi^k_i(\boldsymbol{y}) \mathrm{d}V, \qquad \forall \delta\xi^k_i(\boldsymbol{y}) \in \mathcal{C}_{\#}(Y^f), \tag{14a}$$

$$\int_{Y^f} \frac{\partial \xi^k_i(\boldsymbol{y})}{\partial y_i} \delta\pi^k(\boldsymbol{y}) \mathrm{d}V = 0, \qquad \forall \delta\pi^k(\boldsymbol{y}) \in \mathcal{C}_{\#}(Y^f), \tag{14b}$$

$$\xi^k_i(\boldsymbol{y}) = 0, \qquad \text{on } \Gamma^{sf}, \tag{14c}$$

$$\int_{Y^f} \pi^k(\boldsymbol{y}) \mathrm{d}V = 0. \tag{14d}$$

Cell problem 4: Find the function $\zeta(\boldsymbol{y}) \in \mathcal{C}_{\#}(Y^f)$ such as:

$$\int_{Y^f} \frac{1}{\mathrm{i}\omega \rho^f C^f_p} \kappa^f_{ij} \frac{\partial \zeta(\boldsymbol{y})}{y_j} \frac{\partial \delta\zeta(\boldsymbol{y})}{\partial y_i} \mathrm{d}V + \int_{Y^f} \zeta(\boldsymbol{y}) \delta\zeta(\boldsymbol{y}) \mathrm{d}V$$
$$= \int_{Y^f} \delta\zeta(\boldsymbol{y}) \mathrm{d}V, \qquad \forall \delta\zeta(\boldsymbol{y}) \in \mathcal{C}_{\#}(Y^f) \tag{15a}$$

$$\zeta(\boldsymbol{y}) = 0 \qquad \text{on } \Gamma^{sf}. \tag{15b}$$

The equations (12b), (13b) and (14d) play the role of constraint conditions suppressing rigid modes and assuring the uniqueness of solutions of corresponding cell problems.

3.1.4. Effective properties and macroscopic governing equations

The homogenization method provides effective constitutive relations for averaged fields at the order of ϵ^0. These equations lead to Biot's model of poroelasticity as follows with the disappearance of the superscript $^{(0)}$ for the sake of convenience:

$$\sigma_{ij} = C^*_{ijkl} \varepsilon^s_{kl}(\boldsymbol{x}) - \alpha_{ij} p^f(\boldsymbol{x}), \tag{16a}$$

$$p^f(\boldsymbol{x}) = -M \left[\frac{1}{\mathrm{i}\omega} \frac{\partial w_i}{\partial x_i} + \alpha_{ij} \varepsilon^s_{ij}(\boldsymbol{x}) \right] \tag{16b}$$

where σ_{ij} are the components of the total stress tensor, $w_i = \phi(v^f_i - \dot{u}^s_i)$ with ϕ the porosity, C^*_{ijkl} are the components of the fourth-order drained homogenized stiffness tensor, α_{ij} are

the components of Biot's second-order tensor of effective stress coefficients coupling the solid and fluid phases and M is known as Biot's modulus. These effective properties are determined by means of the solutions of cell problems (see Section 3.1.3) as follows:

$$C^*_{ijkl} = \left\langle c^s_{ijpq}\left(\frac{\partial \chi^{kl}_p(\boldsymbol{y})}{\partial y_q} + \delta_{pk}\delta_{ql}\right)\right\rangle, \tag{17}$$

$$\alpha_{ij} = \phi\delta_{ij} + B_{ij}, \quad B_{ij} = \left\langle c^s_{ijkl}\frac{\partial \beta_k(\boldsymbol{y})}{\partial y_l}\right\rangle = -\left\langle \frac{\partial \chi^{ij}_k(\boldsymbol{y})}{\partial y_k}\right\rangle, \tag{18}$$

$$M = (\phi c + S)^{-1}, \quad S = \left\langle \frac{\partial \beta_k(\boldsymbol{y})}{\partial y_k}\right\rangle \tag{19}$$

where the symbol $\langle * \rangle$ denotes the volume average of $*$ over a representative volume element Y

$$\langle * \rangle = \frac{1}{|Y|}\int_Y * \,\mathrm{d}V \tag{20}$$

with $|Y|$ being the volume of representative volume element and $c = c(\omega)$ is the effective fluid compressibility which is a frequency-dependent function due to the thermal perturbation. This quantity is identified through the solution of the cell problem presented in Eq. (15) as:

$$c = \frac{\gamma^f - (\gamma^f - 1)\phi^{-1}\left\langle \zeta(\boldsymbol{y})\right\rangle}{\gamma^f P^f}. \tag{21}$$

The macroscopic governing equations can be written as:

$$\frac{\partial \sigma_{ij}}{\partial x_j} = -\bar{\rho}\omega^2 u^s_i + \rho^f \mathrm{i}\omega w_i, \tag{22a}$$

$$w_i = -H_{ik}\left(\frac{\partial p^f}{\partial x_k} - \rho^f\omega^2 u^s_k\right), \tag{22b}$$

where $\bar{\rho} = (1-\phi)\rho^s + \phi\rho^f$. Equation (22b) depicts Darcy's generalized law and $H_{ik} = H_{ik}(\omega)$ denotes the components of the effective generalized Darcy second-order tensor [20]. This frequency-dependent quantity is determined through the solution of the cell problem presented in Eq. (14) by the following relation:

$$H_{ik} = \left\langle \xi^k_i(\boldsymbol{y})\right\rangle. \tag{23}$$

The effective dynamic permeability second-order tensor is deduced from the generalized Darcy coefficient through the following relation [21]:

$$k_{ik} = \eta H_{ik}. \tag{24}$$

At the limit $K^f/K^s \to 0$ where K^s and K^f are respectively the static bulk modulus of the solid and fluid phases, the solid phase can be considered as motionless and the poroelastic material can be regarded as a perfect fluid of the equivalent dynamic mass density $\boldsymbol{\rho}_{eq}$ and the equivalent dynamic bulk modulus K_{eq} [18, 22]. Note that $\boldsymbol{\rho}_{eq}$ is a second-order tensor. These two equivalent parameters can respectively be expressed in terms of the effective dynamic mass density $\boldsymbol{\rho}^f_{eff}$ [23] and the effective dynamic bulk modulus K^f_{eff} [24] of the fluid phase as follows:

$$\boldsymbol{\rho}_{eq} = \frac{1}{\phi}\boldsymbol{\rho}^f_{eff}, \qquad K_{eq} = \frac{K^f_{eff}}{\phi}. \tag{25}$$

The effective dynamic bulk modulus K^f_{eff} of the fluid phase is the inverse of the effective fluid compressibility c while the effective dynamic mass density $\boldsymbol{\rho}^f_{eff}$ of the fluid phase can be calculated through the characteristic function $\xi(\boldsymbol{y})$ as:

$$\rho^f_{eff,ik} = \frac{\phi}{\mathrm{i}\omega}\left\langle \xi^k_i(\boldsymbol{y})\right\rangle^{-1}. \tag{26}$$

3.2. Numerical implementation

Cell problems were solved by using the finite element method and simulations were carried out unsing the Comsol Multiphysics software [25]. Cell problems 1 and 2 corresponding to Eqs. (12) and (13) are frequency-independent, whereas cell problems 3 and 4 represented by Eqs. (14) and Eqs. (15) are frequency-dependent. These last two problems need to be solved at each frequency of interest.

After the resolution of cell problems, the characteristic functions corresponding to these problems are determined and the effective properties of the homogenized material can be attained by substituting these functions into Eqs. (17)-(19), (21), (23) and (26).

Cell problems 1 and 2 are solved on the geometry corresponding to the solid phase, whereas the resolution of the two remaining cell problems is conducted on the geometry representing the fluid phase. These geometries are meshed *via* unstructured meshes of quadratic Lagrange tetrahedral elements by respecting periodic constraints between opposite boundaries. For an elementary cube whose the side length is 305 μm, the numbers of degrees of freedom of the solid and fluid phases are about 342×10^3 and 451×10^3, respectively.

4. Construction of idealized representative volume elements

4.1. Construction of idealized elementary pore and matrix

The construction of a unit cell is based on three factors: pore shape, pore entrance dimension and porosity. Because the porous material was obtained after NaCl extraction, or in other words, NaCl particles left the void space constituting the porosity of the material, the pore shape correlates strictly with the shape of NaCl particles. NaCl is an ionic compound made of sodium and chloride atoms. When a number of these molecules get together to form a crystal, they tend to arrange themselves in a cubic pattern. As a result, NaCl crystals are also cubic and this pattern is confirmed by the SEM image of NaCl particles

in Fig. 4a. Considering this fact, the shape of a pore corresponding to a NaCl particle is regarded as cubic; more precisely we have a cubic pore with fillet external edges (see Fig. 4c). It is useful to remember that the fusion of NaCl cubic particles has many contact/fusion modes, namely “face to face", “side to side", “point to point" modes, etc., [26], but the “face to face" mode has been more frequently found in SEM micrographs (see Figs. 2 and 4b); therefore, this mode was chosen to construct the unit cell, leading to square-shaped pore entrances. From the MIP profile, these square entrances are considered to have the side dimension $l_t = 180$ μm (see Fig. 4d). Because of the value of porosity 83% identified by determination of the mass and the volume of a piece of the porous material as described above with the NaCl volume fraction 82%, the unit cell is constructed so that its porosity is 83%. To make the fillet-edge cubic pore, an elementary cube with side length $l = 305$ μm and three orthogonal cylinders with a radius of 177 μm and a length of 305 μm are created with the same center point. The elementary pore is then the intersection of the elementary cube and the three cylinders. By calculating the difference between the elementary cube and the elementary pore, the elementary matrix is obtained (see Fig. 4d). Void space in porous media is described as a network of pores and throats where larger spaces are referred to as pores, which are connected by smaller spaces (constrictions) referred to as throats. Therefore, hereafter, the term “pore size” is used to refer to the length of the elementary cube' side.

4.2. Construction of representative volume elements

In this section, the effect of the unit cell arrangements in the three-dimensional space is introduced in order to study their impact on the effective mechanical, hydraulic and acoustic properties. Based on the geometric configuration of a unit cell made of an idealized elementary pore and matrix constituting the fluid and solid phase presented in section 4.1, four different ordered arrangements of this elementary cell are presented in Fig. 5. These four arrangements result in four distinct representative volume elements described as follows:

- Arrangement 1: the elementary cells are vertically and horizontally aligned;
- Arrangement 2: the elementary cells in the second layer are horizontally offset with to those of the first layer, by a distance $l/2$ along of the sets of rows;
- Arrangement 3: the elementary cells in the second layer are horizontally and vertically offset with to those of the first layer, by a distance $l/2$ along of the sets of rows;
- Arrangement 4: each elementary cell is horizontally offset with to the next cell, by a distance $l/2$ along of the sets of rows.

The choice of these arrangements is, in particular, due to the fact that it maintains the porosity at the same value of 83%, which corresponds to the porosity of the porous material obtained by the elaboration process. Moreover, because the use of the elementary cube as a representative volume element is enough to express arrangement 1 and the symmetry of the cube ensures the periodicity in three directions, the representative volume element in this

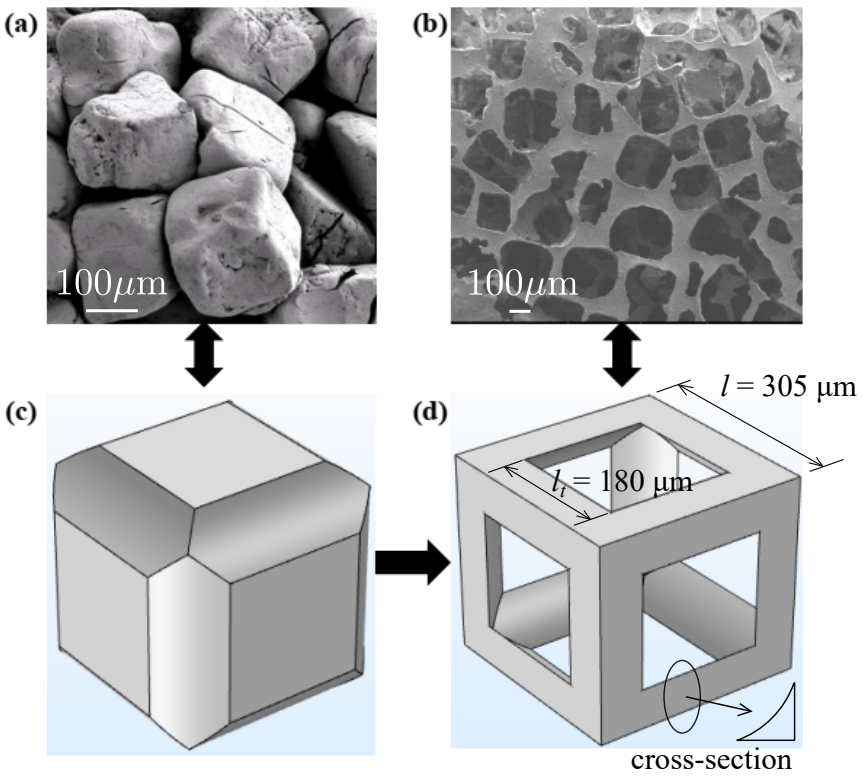

Figure 4: Construction of the elementary pore and matrix by the idealized periodic microstructure. (a) SEM image of sintered NaCl particles; (b) SEM image of the present porous material; (c) Elementary cubic pore; (d) Elementary cubic matrix.

case has a side length of l. For the other arrangements, the corresponding representative volume elements are cubic volumes with a side length of $2l$ and are constructed in a manner so that each arrangement is well represented and the periodic conditions are satisfied. All considered representative volume elements possess the orthotropic symmetry, in which there are 3 mutually orthogonal planes of reflection symmetry; especially, the representative volume element for arrangement 1 refers to the cubic symmetry with also $\pi/2$ rotation symmetry with respect to those planes while the representative volume element for arrangements 3 and 4 involves the transversely isotropy with additional axial symmetry about an axis shown in Fig. 5. It is the axis orthogonal to the square-marked surface for arrangement 3 and to the star-marked surface for arrangement 4.

5. Sound absorption of a poroelastic plate

In order to assess the sound absorption capacity of the elaborated porous material, a normal incidence acoustic problem is considered for a plate of thickness d made of this material with a rigid impervious backing at one side and surrounded by the air from another (see Fig. 6). The problem is described in the Cartesian coordinate system with an orthogonal basis $(\mathbf{e}_1, \mathbf{e}_2, \mathbf{e}_3)$ and the position vector $\boldsymbol{x} = (x_1, x_2, x_3)$. Because the study focuses on the

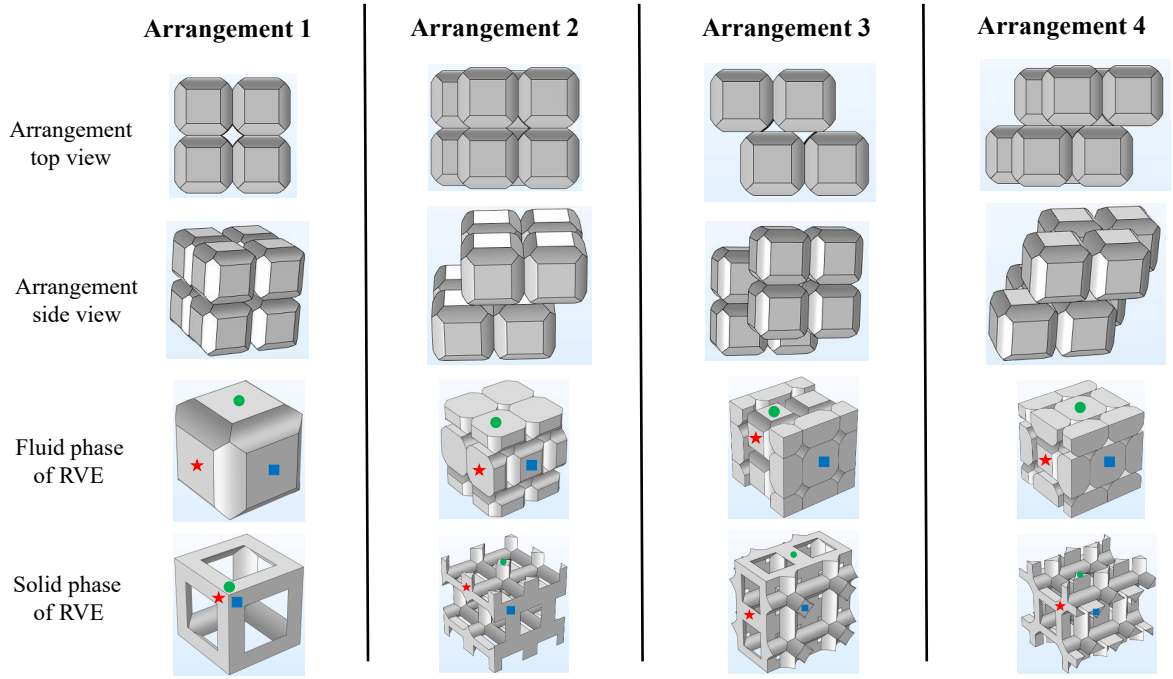

Figure 5: Representative volume elements of the four pore arrangements. The star-, square- and circle-marked surfaces correspond to the surface orthogonal to the incidence direction of the plane pressure described in section 5.

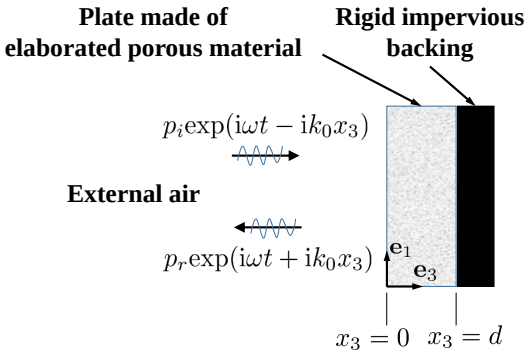

Figure 6: Normal incidence acoustic problem for a plate of thickness d made of the elaborated porous material.

normal incidence, a one-direction problem is considered and the schema in Fig. 6 shows the case of x_3-direction normal incidence. The analytical solution of one-dimensional wave propagation in an anisotropic poroelastic layer coupled with fluids has been derived in [27, 28]. The incident plane pressure wave, depicted by $p_i \exp(\mathrm{i}\omega t - \mathrm{i}k_0 x_3)$ with the amplitude p_i and the wavenumber k_0, strikes the porous plate and is then reflected. The reflected wave field is denoted by $p_r \exp(\mathrm{i}\omega t + \mathrm{i}k_0 x_3)$ where p_r is the amplitude. This problem is described in

detail in [29, 28]. The boundary conditions associated with this problem are the followings:

$$\sigma_{33} = -p^{(n)},\ p^f = p^{(n)},\ \mathrm{i}\omega u_3^s + w_3 = v^{air} \quad \text{at } x_3 = 0, \tag{27}$$

$$u_3^s = 0,\ w_3 = 0 \quad \text{at } x_3 = d, \tag{28}$$

where $p^{(n)} = p_i \exp(\mathrm{i}\omega t - \mathrm{i}k_0 x_3) + p_r \exp(\mathrm{i}\omega t + \mathrm{i}k_0 x_3)$ and v^{air} are respectively the pressure field and the velocity of the external air. By introducing the surface impedance Z_s defined by $Z_s = p^{(n)}(0)/v^{air}(0)$ at $x_3 = 0$ and applying the boundary conditions (27) and (28) to the macroscopic governing equations (22), the surface impedance Z_s can be determined. In a normal incidence problem, the reflection coefficient R which is generally defined as the ratio p_r/p_i can be calculated from the surface impedance through the following relation [30]:

$$R(\omega) = \frac{Z_s - Z_0}{Z_s + Z_0}, \tag{29}$$

where $Z_0 = \rho_0 c_0$ is the characteristic impedance of the air with ρ_0 the density of the air at rest and c_0 the sound velocity in the air. Subsequently, the absorption coefficient α_a is determined by [30]:

$$\alpha_a(\omega) = 1 - |R|^2. \tag{30}$$

6. Numerical results and discussion

In this section, the effect of pore arrangements, porosity and pore size on effective mechanical, hydraulic and acoustic properties are presented and discussed in order to improve the performances of this new bio-based porous material. By conducting three-microphone impedance tube experiments on the porous material, the measured effective acoustic properties are discussed in comparison with the modeling results.

6.1. Effect of pore arrangements on effective properties

The epoxy matrix is isotropic and its tensor c^s_{ijkl} of elastic properties is characterized by two independent coefficients, Young's modulus $E^s = 4.5 \times 10^9$ Pa and Poisson's ratio $\nu^s = 0.34$. Its density is given by $\rho^s = 1318$ kg/m^3. The fluid phase is taken to be the air with following properties: $\rho^f = 1.225$ kg/m^3, $\eta = 1.81 \times 10^{-5}$ Pa.s, $\kappa_0^f = 2.41 \times 10^{-2}$ W/(m.K), $\gamma^f = 1.4$ at $P^f = 101325$ Pa. The sound velocity in the air is given as $c_0 = 331.6$ m/s.

Note that with these data and with a frequency ranging from 4 to 4500 Hz, the associated wavelength λ varies in the range given by $[0.638, 7.981]$ (in meter) in the poroelastic domain. These values show that the scale separation condition necessary for the relevance of the homogenization-based modelling which requires $\lambda \gg \ell_R$, where $\ell_R \sim 0.60 \times 10^{-3}$ m is the representative volume element size, is well respected.

In the case of arrangement 1, the numerical results of effective elasticity tensor $\boldsymbol{C}^*$ in the Voigt notations and Biot's tensor $\boldsymbol{\alpha}$ are as follows:

$$\boldsymbol{C}^* = \begin{bmatrix} 332.9 & 34.4 & 34.4 & 1.6\times10^{-3} & -5.9\times10^{-3} & -34.3\times10^{-3} \\ & 332.9 & 34.4 & -13.4\times10^{-3} & 4.5\times10^{-3} & -31.1\times10^{-3} \\ & & 332.9 & -10.1\times10^{-3} & -10.0\times10^{-3} & 9.5\times10^{-3} \\ & & & 21.0 & -3.3\times10^{-3} & -1.6\times10^{-3} \\ & \text{sym.} & & & 21.0 & -1.9\times10^{-3} \\ & & & & & 21.0 \end{bmatrix} \text{(MPa)}$$

$$\boldsymbol{\alpha} = \begin{bmatrix} 0.969 & 43.63 \times 10^{-7} & 8.94 \times 10^{-7} \\ & 0.969 & 17.07 \times 10^{-7} \\ \text{sym.} & & 0.969 \end{bmatrix}$$

Regarding frequency-dependent properties, namely Biot's modulus M, the effective compressibility c and the effective dynamic permeability tensor $\boldsymbol{k}$, their values at frequency of 10 Hz read:

$$M = (0.12 + \mathrm{i}4.08 \times 10^{-4}) \times 10^{6} \ \text{(Pa)} \tag{31}$$

$$c = (9.87 - \mathrm{i}\,0.03) \times 10^{-6} \ (\text{Pa}^{-1}) \tag{32}$$

$$\boldsymbol{k} = \begin{bmatrix} 1.05 \times 10^{-9} & 2.06 \times 10^{-13} & 8.71 \times 10^{-13} \\ & 1.05 \times 10^{-9} & 9.68 \times 10^{-13} \\ \text{sym.} & & 1.05 \times 10^{-9} \end{bmatrix} \tag{33}$$

$$- \mathrm{i} \begin{bmatrix} 1.01 \times 10^{-11} & 2.42 \times 10^{-15} & 1.25 \times 10^{-14} \\ & 1.01 \times 10^{-11} & 1.39 \times 10^{-14} \\ \text{sym.} & & 1.01 \times 10^{-11} \end{bmatrix} \ (\text{m}^2) \tag{34}$$

It can be seen that the form of tensors $\boldsymbol{C}^*$, $\boldsymbol{\alpha}$ and $\boldsymbol{k}$ reflects well the cubic symmetry of the representative volume element in the case of arrangement 1 for which the tensor $\boldsymbol{C}^*$ has 3 independent coefficients while two tensors $\boldsymbol{\alpha}$ and $\boldsymbol{k}$ are diagonal with $\alpha_{11} = \alpha_{22} = \alpha_{33}$ and $k_{11} = k_{22} = k_{33}$.

More generally, it is assumed that the representative volume elements associated with 4 arrangements are taken so that their star-, square- and circle-marked surfaces are orthogonal to $\mathbf{e}_1$-, $\mathbf{e}_2$- and $\mathbf{e}_3$-direction, respectively, and the indices for components of effective tensors are determined accordingly. In a general orthotropic case, the effective elasticity tensor $\boldsymbol{C}^*$ has 9 independent components and Biot's tensor $\boldsymbol{\alpha}$ has a diagonal form with 3 independent components. Table 1 shows 9 components of the effective elasticity tensor and the diagonal components of Biot's tensor for the 4 cases of pore arrangements. It is easily seen that the results reflect well the form of the elasticity tensor and Biot's tensor resulting from the arrangements' symmetry. While the elasticity tensor possesses 9 independent components and Biot's tensor has 3 independent components for arrangement 2, corresponding to the general orthotropic symmetry, the elasticity and Biot's tensors for the arrangements 3 and 4 reflect the transversely isotropy with 5 and 2 independent components, respectively. Particularly, in Tab. 1, while the homogenized materials are generally more resistant to tension than to shear and most of modulus components as well as components of Biot's tensor do not vary strongly according to pore arrangements, a noticeable drop in tension modulus C^*_{22} along with a sharp rise in shear modulus C^*_{55} in case of arrangement 3 implies a degradation of tension resistance and an improvement in shear resistance of the material related to the axis of transverse isotropy corresponding to arrangement 3.

Table 1: Non-zero components of effective elasticity tensor $\boldsymbol{C}^*$ in the Voigt notations and Biot's tensor $\boldsymbol{\alpha}$ in different cases of pore arrangements.

		Pore arrangements			
		1	2	3	4
Components of tensor $\boldsymbol{C}^*$ (10^6 Pa)	C^*_{11}	332.9	341.9	381.4	346.6
	C^*_{22}	332.9	364.3	141.9	324.0
	C^*_{33}	332.9	214.6	381.0	324.0
	C^*_{44}	21.0	15.1	23.8	11.4
	C^*_{55}	21.0	33.9	90.7	37.5
	C^*_{66}	21.0	38.0	23.8	37.5
	C^*_{12}	34.4	45.0	59.1	49.7
	C^*_{13}	34.4	56.2	86.1	49.7
	C^*_{23}	34.4	25.3	59.1	62.0
	Symmetry	cubic	orthotropic	orthotropic	orthotropic
Components of tensor $\boldsymbol{\alpha}$	α_{11}	0.969	0.965	0.959	0.965
	α_{22}	0.969	0.966	0.980	0.966
	α_{33}	0.969	0.977	0.959	0.966

In Figs. 7 and 8, we present respectively results of the effective dynamic permeability and effective dynamic compressibility. The absorption characteristics of the considered porous materials are quantified using the complex values of these two parameters. The presence of components of the permeability tensor in Fig. 7 indicates the properties of this tensor and reflects the symmetry type corresponding to each arrangement. For instance, in the case of arrangement 1, the permeability tensor is spherical for which $k_{11} = k_{22} = k_{33}$, implying the cubic symmetry, whereas for arrangement 4, the tensor has a diagonal form with 2 independent components, representing the transversely isotropy. Comparing the permeability results for arrangement 1 with those for other arrangements, one can notice that while arrangements 2, 3 and 4 have the permeability component *versus* frequency curves with similar corresponding patterns, the curves for arrangement 1 follow their own specific patterns and there is a difference of at least 10 times between the permeabilities for arrangement 1 and those for the others. In addition, regarding the two arrangements corresponding to the transverse isotropy, an attention is also paid to the fact that the permeability component related to the axis of rotation symmetry has the lowest absolute value compared with two other components in case of arrangement 3 and inversely has the highest absolute value in case of arrangement 4. Regarding compressibility, Fig. 8 shows that the results for the three arrangements 2, 3 and 4 prove to be similar, while being slightly different from the compressibility for arrangement 1. This reveals that the arrangements have not much influence on the compressibility of the materials.

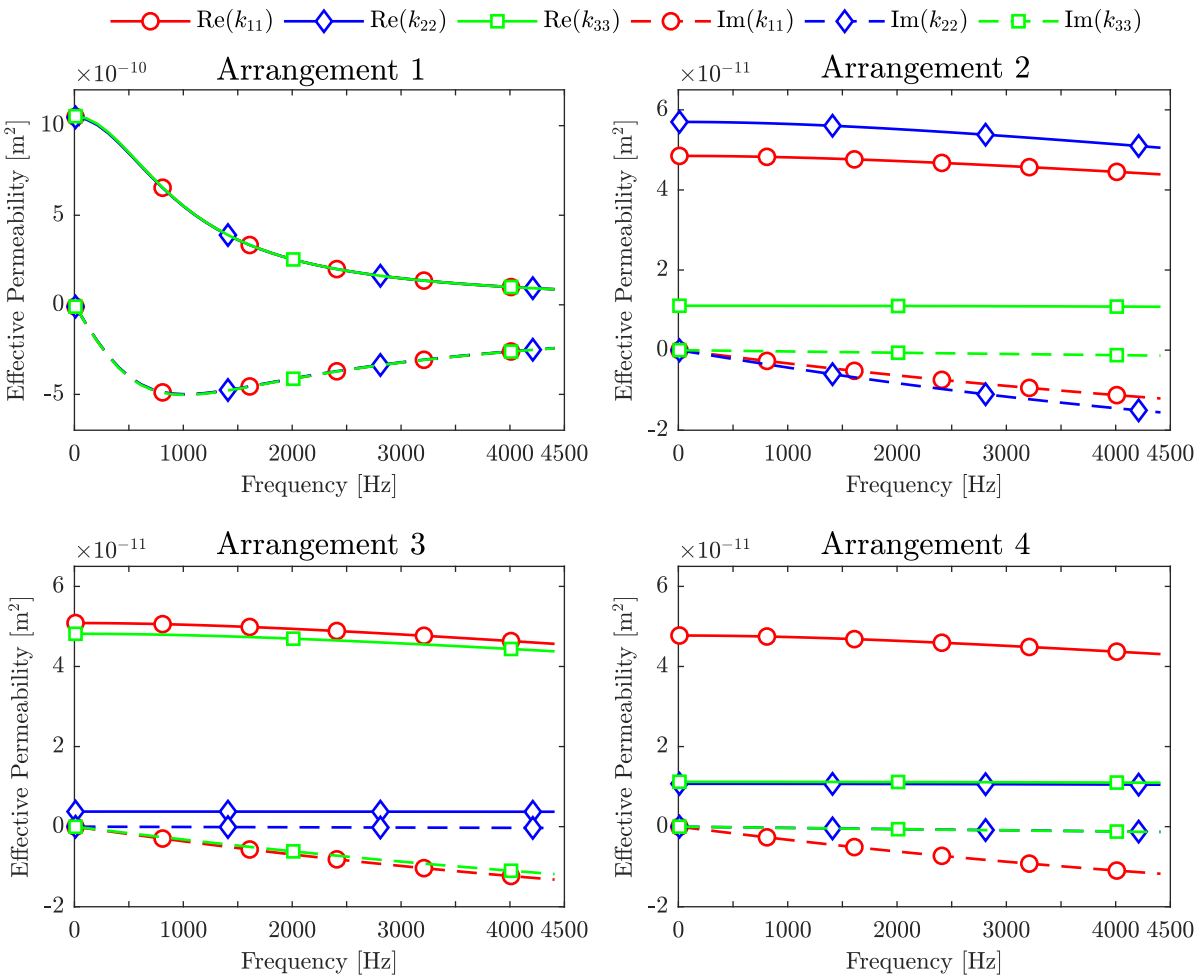

Figure 7: Dependence of non-zero components of the effective dynamic permeability tensor on different pore arrangements.

6.2. Effect of pore arrangements on sound absorption of a poroelastic plate

The dependence of sound absorption on pore arrangements is illustrated in Fig. 9. In this figure, the sound absorption coefficient has been calculated for different orientations of the incident plane pressure wave, which is orthogonal to the star-, square- and circle-marked surfaces defined in Fig. 5. From Fig. 9, it can be noted again that the symmetry characteristics are well represented. Arrangement 1 with cubic symmetry gives the material with the same sound absorption coefficients for all three directions. Two arrangements with transverse isotropy result in materials of which sound absorption coefficients are the same for 2 directions orthogonal to the axis of rotation symmetry. Surprisingly, in case of arrangement 2, despite the difference in components related to $\mathbf{e}_1$ and $\mathbf{e}_2$ directions of the elasticity tensor, Biot's tensor as well as the permeability tensor, the sound absorption behaviours corresponding to these directions are relatively close to each other. Concerning arrangements 2, 3 and 4, one can also observe that the sound absorption is the best at

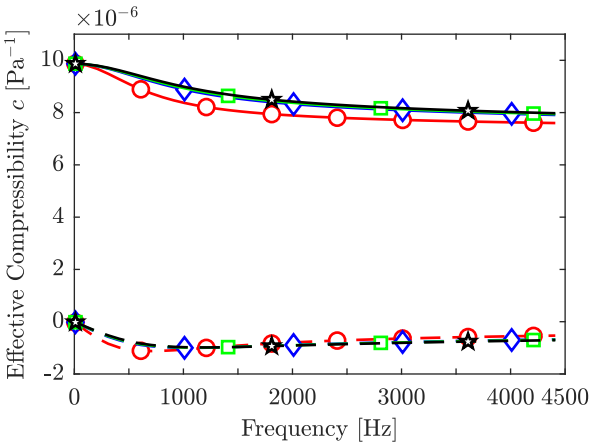

Figure 8: Dependence of the effective dynamic compressibility on different pore arrangements. Solid lines with circular, diamond, square and star markers represent respectively real parts of compressibility in case of arrangements 1, 2, 3 and 4. Dashed lines with circular, diamond, square and star markers represent respectively imaginary parts of compressibility in case of arrangements 1, 2, 3 and 4.

low frequencies in directions corresponding to a permeability smaller than those in other directions; inversely, the dominance of sound absorption is recorded at high frequencies in directions corresponding to a larger permeability. The fact that the compressibility values are similar for these three cases implies that the permeability, not the compressibility, is the key parameter resulting in the different sound absorption behaviours related to different placements of unit cells. Regarding arrangement 1 and in the frequency range of interest, one may notice the smallness of the sound absorption coefficient in this case, compared with those in other arrangements in spite of the fact that the permeability for this arrangement is much higher than those for other configurations. Normally, the increase in the permeability implies the entrance of more sound waves and hence the possibility of more attenuated sound energy. This result has to be relativized since it is generally valid for relatively large thicknesses. Nonetheless, besides higher permeability, the microstructure of the material resulting from arrangement 1 has also a larger pore entrance dimension compared to those for other configurations. This leads to the decrease of viscous damping and thermal dissipation, and therefore, results in the less effective sound absorption. This phenomenon is also observed in some parametric studies carried out in two dimensions for fibrous media [31] as well as in three dimensions for foams [14]. Because the pore arrangement duplicates the arrangement of porogen particles, we can link the porogen arrangement and the sound absorption. Although the porogen arrangement is not controlled yet in the present elaboration processing, the results of this section suggest that the arrangement of porogen particles should fall into types 2, 3 or 4 for the possibly highest sound absorption.

6.3. Experimental validation

6.3.1. A comparison of acoustic properties

The validation of the model is performed by using three-microphone impedance tube experiments on the porous material for which the acoustic properties are measured. The

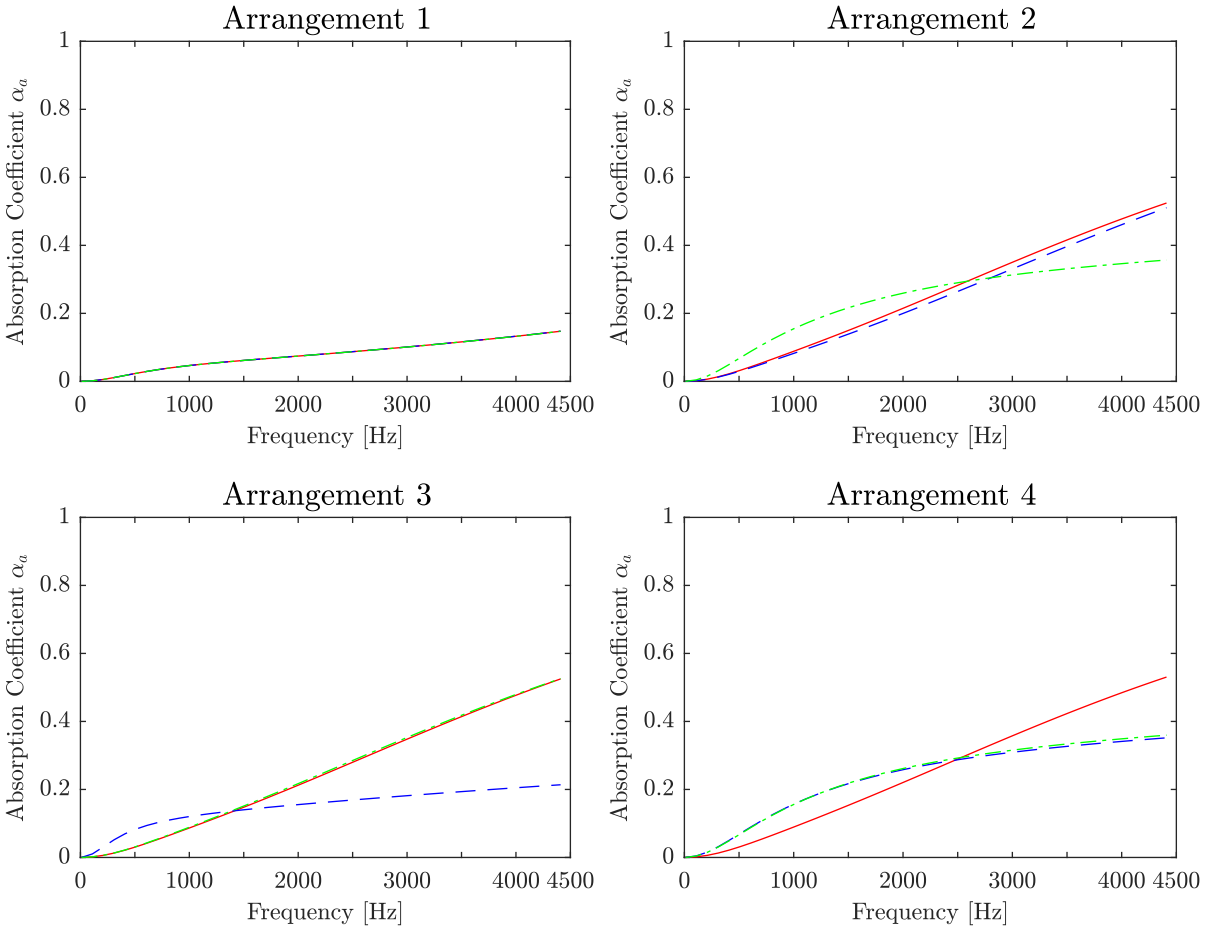

Figure 9: Dependence of sound absorption coefficients on different pore arrangements. The plate thickness is 0.5 cm. Solid, dashed and dashed-dot lines correspond to cases in which star-, square- and circle-marked surfaces of representative volume elements are orthogonal to the normal incidence direction, respectively.

configuration of the experiments is shown in Fig. 10. Two samples having the cylindrical shapes with a diameter of 4 cm and a thickness of 0.5 cm were tested. For each sample, two experiments were conducted for two opposite incidence surfaces. The tests were carried out with a frequency ranging from 4 to 4500 Hz, under rigid impervious backing conditions and normal incidence with acoustic plane waves. Three microphones measure the acoustic pressures at their positions and the data are transferred to the computer equipped with the TubeCell software developed by Matelys Resesarch Lab. This software analyses the pressure data and computes acoustic properties such as the sound absorption coefficient, the reflection coefficient, the surface impedance, the equivalent dynamic mass density and the equivalent dynamic bulk modulus [32].

The experimental results are plotted in Figs. 11 to 13. For comparison purposes, these figures also show the results obtained *via* the model described in this paper by using the arrangement 1 which allows a best approximation to the effective parameters of interest.

In these figures, the experimental results are represented by their mean values alongside

the corresponding error bars at each frequency. The green and cyan colours are used for the standard deviation.

A standardized measure of the dispersion is given by the coefficient of variation which is also called relative standard deviation. The measure is expressed as a percentage and is defined as the ratio of the standard deviation to the mean. This measure of the dispersion is used in what follows for the acoustic properties.

In Fig. 11 (left), for real and imaginary parts of Z_s, the maximum values of relative standard deviation are about 55% and 13% respectively.

In Fig. 11 (right), for real and imaginary parts of R, the maximum values of relative standard deviation are about 6% and 4.5% respectively.

In Fig. 12, the maximum value of relative standard deviation of α_a is about 15.9%.

In Fig. 13 (left), for real and imaginary parts of $\rho_{eq,33}$, the maximum values of relative standard deviation are about 61.6% and 57.7% respectively.

In Fig. 13 (right), for real and imaginary parts of K_{eq}, the maximum values of relative standard deviation are about 13.2% and 22.7% respectively.

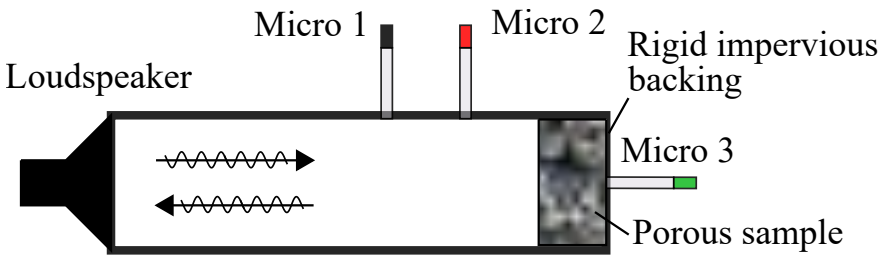

Figure 10: Sketch of experimental setup of three-microphone impedance tube experiment.

In Figs. 11 and 12, it can be seen that the model slightly underestimates the values of absorption coefficient, corresponding to a little overestimation of the real part of the values of reflection coefficient. The discrepancy is greater for higher frequencies. On the contrary, a good match between model and experimental results is captured for frequencies higher than 100 Hz for the values of surface impedance, whereas for lower frequencies, the experimental values of surface impedance exhibit a fluctuation, and accordingly, a mismatch between model and experimental results. From both model and experimental results, we can observe that the absorption coefficient tends to increase when the frequency increases. This observation is in accordance with the decrease in the module of the reflection coefficient and the surface impedance with respect to the increase of the frequency.

The comparison is also carried out in terms of the equivalent dynamic density and the equivalent dynamic bulk modulus (see Fig. 13). A good agreement between model and experimental results is figured out for these two parameters in the frequency range higher than 100 Hz. When the frequency is lower than this value, there are fluctuations in the experimental values of both parameters and accordingly the model's results deviate from the experimental ones. The divergences observed for these two equivalent parameters, but also for the surface impedance, may be attributed to a lack of accuracy due to edge constraints on small samples. Additionally, the mismatch in the frequency range lower than 100 Hz may

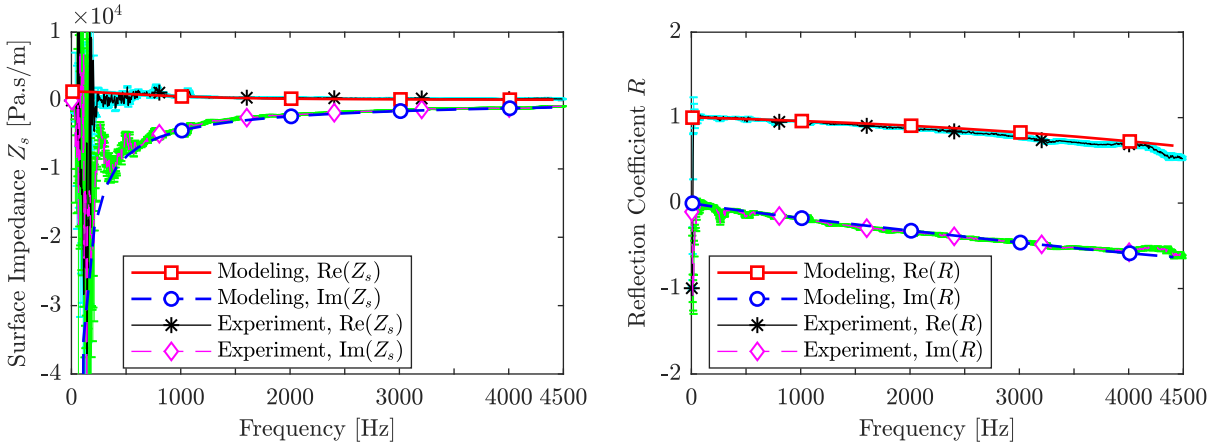

Figure 11: Comparison of model and experimental results of surface impedance Z_s (left) and normal incidence reflection coefficient R (right). The sample thickness is 0.5 cm. The green and cyan colours are used for the standard deviation.

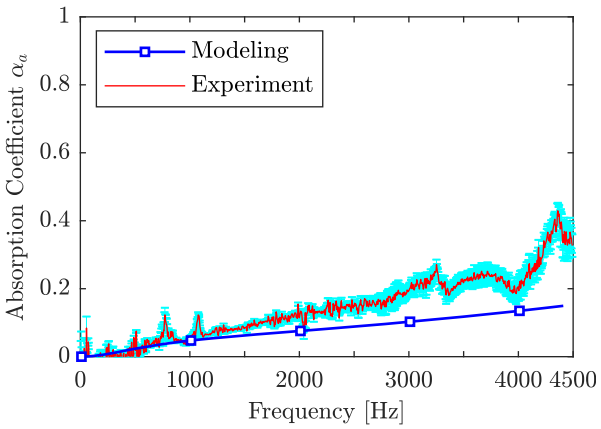

Figure 12: Comparison of model and experimental results of normal incidence absorption coefficient α_a (see eq. (30)). The sample thickness is 0.5 cm. The green colour is used for the standard deviation.

be explained by the dependence of the three-microphone impedance tube testing on the upstream microphones inter-spacing, which becomes too small compared to large wavelengths and degrades the accuracy of the testing method [32].

6.3.2. Interpretation of the differences between experimental and modeling results

In order to further investigate the observed discrepancies between model and experimental results of the absorption coefficient in the high frequency range, an important step is to understand how transport properties depend on the details of the porous microstructure. From the periodic unit cell describing the idealized pore structure of the porous material (see Fig. 4d), we first proceed to numerically solve the appropriate transport equations (Stokes hydrodynamic equations for viscous fluid flow, potential equations for non-viscous fluid flow,

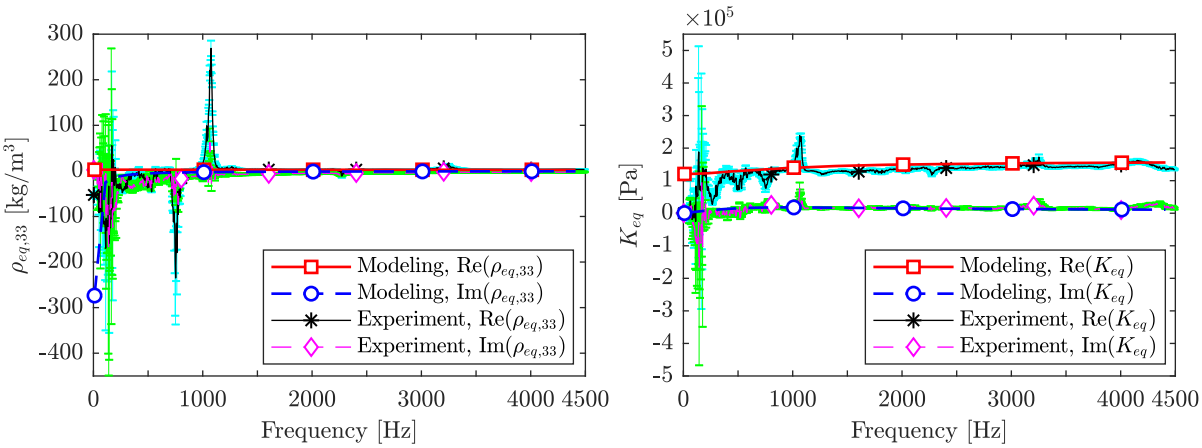

Figure 13: Comparison of numerical and experimental results of equivalent dynamic density component $\rho_{eq,33}$ (left) and equivalent dynamic bulk modulus K_{eq} (right). The sample thickness is 0.5 cm. The green and cyan colours are used for the standard deviation.

Poisson equations for heat diffusion) in order to provide a description of the transport processes in the modeled porous material [31, 14]. Then, an experimental characterization of the transport parameters is also obtained from acoustic measurements [23, 24]. Table 2 shows a comparison between experimentally and numerically determined transport parameters.

It should be noted that the viscous characteristic length Λ [33] is a pore-volume-to-surface ratio of the pore-solid interface in which each area or volume element is weighted according to the local value of the non-viscous fluid flow field.

Table 2: Effective properties including purely geometrical and transport properties determined numerically from the arrangement 1 and compared with the experimental results.

	ϕ	Λ (μm)	k (m^2)
Simulation	0.83	112	10.1×10^{-10}
Experiment	0.83 ± 0.02	36 ± 23	$(10.1 \pm 3.0) \times 10^{-10}$
	α_∞	Λ' (μm)	k' (m^2)
Simulation	1.23	203	22.6×10^{-10}
Experiment	1.23 ± 0.57	84 ± 24	$(11.0 \pm 6) \times 10^{-10}$

Consequently, the quantity Λ has the dimension of length and gives a good estimate of the smallest interconnections between pores, because of a weighting procedure implied in its definition. The experimental value of Λ is about a third of the numerical one obtained with the idealized unit cell, revealing that the observable disorder in Figs. 4a) and 4b) reduces significantly the interconnection between open pores. The experimental value of the tortuosity α_∞ [34] is in agreement with the one actually computed. The thermal characteristic length Λ' [35] is another factor like Λ above, but without weighting and is therefore

a simple length scale that characterizes, in some way, the pore diameter. Comparing the numerical and experimental values of the thermal characteristic length Λ', it can be seen that the experimental value of the effective pore diameter is lower than the one given by the idealized model. Figures 4a) and 4b) show a surface roughness increasing the surface area of the pore-solid interface, which has the effect of decreasing the overall pore-volume-to-surface ratio. We note that the other measured macroscopic parameters, namely the porosity ϕ and the static viscous permeability k, are in agreement with the computed ones. Also worth being noted, the characterized static thermal permeability k' [36], which should satisfy the inequality $k' \geq k$, is close to the value of the static viscous one. Johnson *et al.* [34] and Lafarge *et al.* [36] showed that the equivalent dynamic density $\rho_{eq,33}(\omega)$ and the equivalent dynamic bulk modulus $K_{eq}(\omega)$ can be adequately described by approximate but robust semi-phenomenological models based on these macroscopic parameters $\phi, \Lambda', k, \alpha_\infty, \Lambda$ and k'. The better agreement between the numerically characterized and measured behaviour of the sound absorption is indicative of the fact that the periodic unit cell captures most of the physics of the visco-thermal exchanges, but that a more accurate representation of the high frequency behaviour could eventually be obtained by introducing a disorder in the pore space.

6.4. Effect of porosity

In order to investigate the influence of porosity on effective properties and acoustic behaviour of the material, three cases of porosity, namely 69%, 83% and 96%, are under consideration in the context of arrangement 1 in which the elementary pore and matrix play the role of the unit cell. The porosity is varied in a manner so that the pore size remains unchanged. Note that in this paper, the pore size means side length of the elementary cube, hence referring also to the size of the unit cell in case of arrangement 1, that is $l = 305$ μm.

6.4.1. Effect of porosity on effective properties

The porosity-dependence of independent components of effective elasticity tensor $\boldsymbol{C}^*$ and Biot's tensor $\boldsymbol{\alpha}$ is shown in Tab. 3. When the porosity increases, the *moduli* of the elasticity tensor $\boldsymbol{C}^*$ decrease, particularly the shear components. At the porosity of 96%, the porous material nearly looses its shear resistance. This is attributed to the fact that when the porosity increases, the thickness of the matrix ligaments accordingly decreases, leading to the drop of the *moduli* of the porous material. On the contrary, the increase in the porosity is followed by the increase in components of Biot's tensor $\boldsymbol{\alpha}$. This phenomenon is explained by the fact that higher porosity facilitates an easier fluid flow, favouring the increase in Biot's effective stress coefficients [37].

The dependence of the effective dynamic permeability and the effective dynamic compressibility on the porosity is presented in Fig. 14. It can be seen that the increase in the porosity leads to the increase in the effective permeability, especially at low frequencies. This variation of the permeability with respect to the porosity is explained by the fact that increasing porosity encourages more fluid travelling through pore space, implying the increase in the permeability. Regarding the effective compressibility, this parameter tends to

Table 3: Independent components of effective elasticity tensor $\boldsymbol{C}^*$ in the Voigt notations and Biot's tensor $\boldsymbol{\alpha}$ in different cases of porosity ϕ.

	ϕ	69%	83%	96%
Components of tensor $\boldsymbol{C}^*$ (10^6 Pa)	C^*_{11}	783.7	332.9	60.4
	C^*_{44}	117.1	21.0	0.6
	C^*_{12}	135.8	34.4	2.3
Component of tensor $\boldsymbol{\alpha}$	α_{11}	0.92	0.97	1

decrease when the porosity increases in almost the whole considered frequency range. This trend can also be found in the experimental results for various rock types as shown in [38].

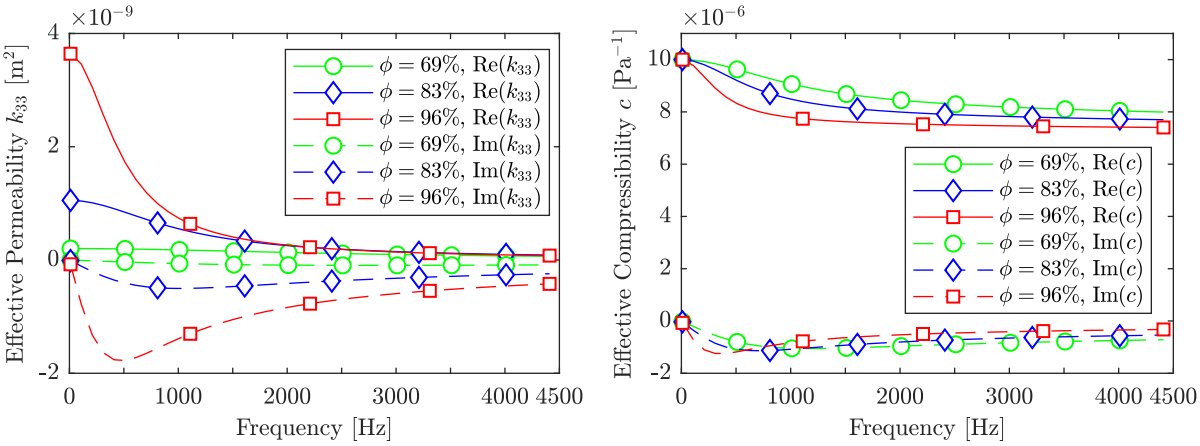

Figure 14: Dependence of the effective dynamic permeability (left) and the effective dynamic compressibility (right) on porosity.

6.4.2. Effect of porosity on sound absorption

The effect of porosity on the sound absorption coefficient of the material is highlighted by Fig. 15. It can be remarked that the absorption coefficient increases slightly with respect to the rise of the porosity within the range of frequencies lower than approximately 1000 Hz, whereas the noticeable improvement on the sound absorption is accompanied by the decrease of the porosity for higher frequencies. In the process of making the porous material by using the Spark Plasma Sintering (SPS) technique, the resulting porosity depends on the pressure and temperature. Higher pressure and higher temperature normally induce a sintered porogen template with more porogen constituents in a volume than in case of a template resulting from a process with lower pressure and lower temperature [39, 15], meaning higher-porosity materials in case of higher pressure and higher temperature. The results of this section suggest that to promote a better sound absorption at frequencies lower than 1000 Hz, we

need to augment the pressure and the temperature during the SPS processing for a material with more porosity. Inversely, for the range of higher frequencies, a decrease of pressure and temperature should be applied during the SPS processing to reduce the porosity and accordingly favour the sound absorption performance of the resulting porous material. Nevertheless, the pressure and the temperature should not be too low in order to allow porogen fusion and ensure the pore interconnection. This implies the existence of optimal pressure and temperature during the SPS processing for attainment of interconnected-pore materials with the best sound absorption performance at higher frequencies.

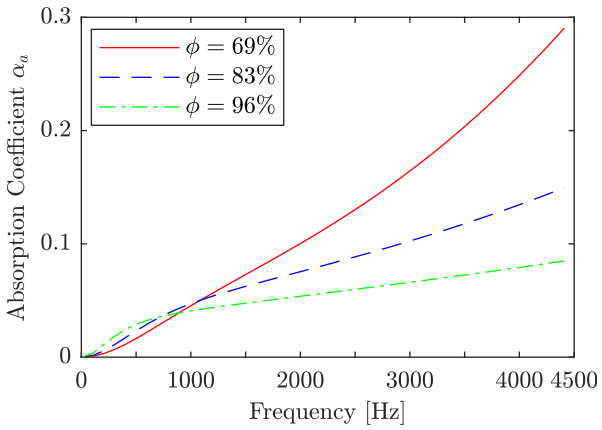

Figure 15: Dependence of sound absorption coefficient on porosity. The plate thickness is 0.5 cm.

6.5. Effect of pore size

In order to understand the relation between the pore size and effective properties as well as the acoustic behaviour of the resulting material, simulations are conducted, in which arrangement 1 is considered and the pore size is varied while maintaining the porosity at 83%.

6.5.1. Effect of pore size on effective properties

In this study, the pore size is linked to the cell size. Within the framework of homogenization method, the effective elasticity tensor $\boldsymbol{C}^*$ and Biot's tensor $\boldsymbol{\alpha}$ are modified by the porosity, not by the cell size or pore size. Nevertheless, the change of pore size or cell size influences both the effective dynamic permeability and effective dynamic compressibility as shown in Fig. 16 where the variation of these properties with respect to the frequency corresponding to three different pore sizes of 45, 350 and 710 μm are presented. It can be noted that at very low frequencies (inferior to 500 Hz), the larger the pore size, the higher the permeability. This is explained by the fact that in case of a larger pore size, more entrance of the fluid through the material is possible, favouring higher permeability. However, in the range of higher frequencies, the permeabilities become lower and closer to each other except that the permeability, in case of the smallest pore size, *i.e.*, 45 μm, remains very low and proves to be unchanged in the whole frequency range. Similarly to the permeability, the

compressibility remains nearly unchanged according to frequency in case of 45 μm pore size. On the contrary, the compressibility in cases of 350 and 710 μm pore size becomes lower and closer to each other when the frequency moves to the higher range. The very low values of the imaginary parts of both permeability and compressibility at high frequencies imply low viscous and thermal dissipation, hence low sound absorption of the material within this frequency range.

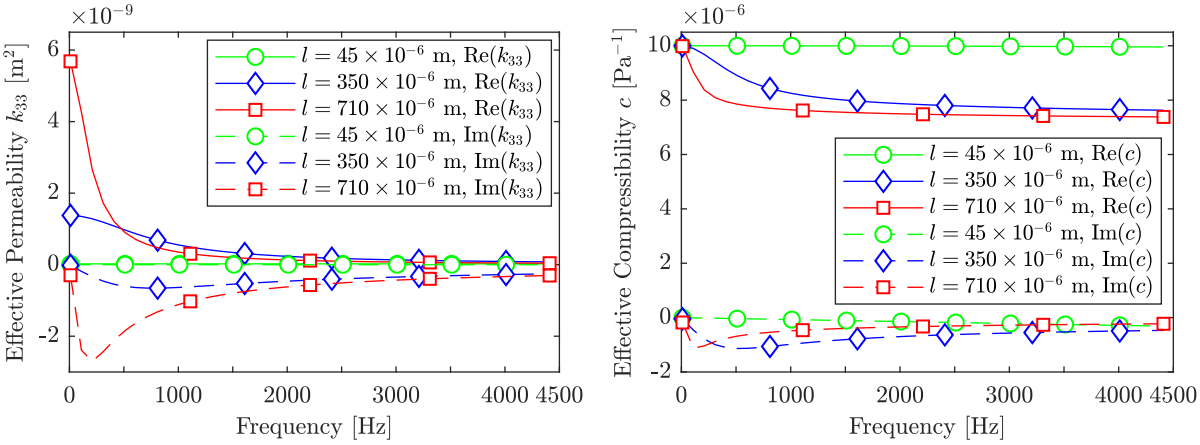

Figure 16: Dependence of the effective dynamic permeability (left) and the effective dynamic compressibility (right) on pore size. The porosity is fixed at $\phi = 83\%$.

6.5.2. Effect of pore size on sound absorption

According to the elaboration process, the pores are obtained by the porogen removal, so the pore size can be considered ideally equal to the porogen size, that is, NaCl particle size. Based on the sieve sizes available on the market for sieving NaCl particles, a variation of the pore size from 45 to 710 μm with a step of 5 μm is taken into account and the normal incidence sound absorption average SAA suggested in the standard ASTM C423 [40] is calculated for each case of the pore size to evaluate the sound absorption capacity of the material at low frequencies. This single number rating is defined as the average, rounded off to the nearest 0.01, of the sound absorption coefficients of a material for the twelve one-third octave bands from 200 through 2500 Hz inclusive, namely 200, 250, 315, 400, 500, 630, 800, 1000, 1250, 1600, 2000 and 2500 Hz according to the relation given by:

$$SAA = \frac{1}{12} \sum_{f_i=200}^{2500} \alpha_a(f_i). \tag{35}$$

Note that in this case, the associated wavelength varies in the range given by $[0.338, 7.981]$ m. Because the sound absorption of a porous material is generally greater at higher frequencies, limiting the frequencies up to 2500 Hz is generally enough to investigate and evaluate the sound absorption performance of the material.

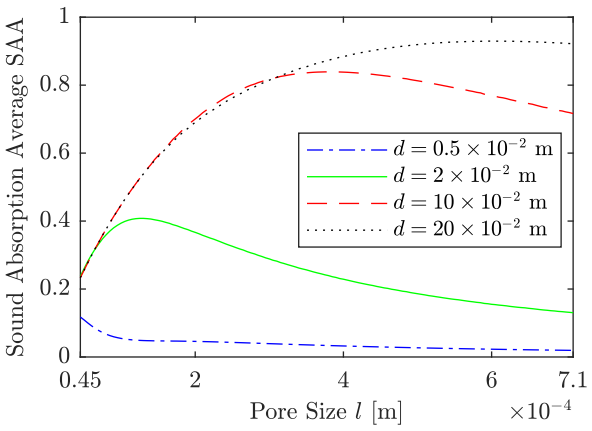

Figure 17: Normal incidence sound absorption average SAA for different cases of the pore size and the porous plate's thickness. The porosity is fixed at $\phi = 83\%$.

The SAA varies in the range of 0 to 1: SAA = 0 indicates a perfect sound reflection and SAA = 1 indicates a perfect sound absorption [41]. The use of the single number rating SAA is a convenient means to provide the insights into the acoustic behaviours of the material within a wide range of pore size and allows to compare different sound absorption performances corresponding to the pore size range of interest. The results of these simulations are presented in Fig. 17 where the variation of SAA for different cases of the pore size and the porous plate's thickness is illustrated.

It is noted that when the plate thickness is 0.5 cm, the SAA is relatively low with the maximum value of 0.12 at the pore size of 45 μm. With this plate, when the pore size increases, the SAA generally follows a decreasing trend. This phenomenon is explained by the fact that the increase in the pore size encourages the enlargement of the cross-sectional area of the fluid phase and hence decreases the viscosity effect as well as the thermal dissipation, leading to the reduction in the sound absorption capability [18]. Note that for the configuration composed of the porous plate and the rigid backing, one of the key parameters is the resistance which is the product of the plate thickness by the static flow resistivity representing the difficulty of the propagation of sound in porous materials. The thinner the plate, the higher the resistivity, and inversely. In the present case, because the plate thickness is not much, the resistivity is generally high, explaining the weak absorption of the material.

When the plate becomes thicker, *i.e.* 2, 10 and 20 cm thickness, the SAA is noticeably improved. For the case of 2 cm thickness plate, the SAA attains its maximum value of 0.41 at the pore size of 120 μm while its minimum value is 0.13 at 710 μm pore size. For 10 and 20 cm thickness plates, the SAA reaches its maximum values of 0.84 and 0.93 at pore sizes of 365 and 600 μm, respectively. This improvement in sound absorbing performance comes from the fact that the increase in the plate thickness makes the propagation of sound waves from the front to the back of the plate face more obstacles, meaning that more sound energy is attenuated. Furthermore, in these three cases of plate thickness, we can observe the

peaks of the pore size *versus* SAA curves. For the range of the pore size on the right-hand side of the peaks, the increase in the pore size is accompanied by the decrease of the SAA, whereas an inverse trend is observed on another side. The explanation of this phenomenon can be deduced by noting again that the principle of sound absorption of porous materials is that the material permits the propagation of sound waves and then the sound energy is attenuated inside the porous materials mainly by the viscous damping and the thermal dissipation. For the range of the pore size on the left-hand side of the peaks, the increase of the pore size leads to the entrance of more sound waves, and up to the values of the pore size corresponding to the peaks, the thickness of the plate as well as the viscous and thermal effects are still important to afford these entering sound waves, meaning that the more entering sound waves, the more attenuated sound energy. On the contrary, on the right-hand side of the peaks, when the pore size increases, the cross-section of the fluid phase proves to be too large, leading to the decrease of viscous damping and thermal dissipation and therefore resulting in less effective sound absorption for a given thickness. The existence of the above-mentioned peaks with two opposite trends is also well documented in [14] with Kelvin's cell (tetrakaidecahedron) for high porosity foams and in [42] for pores of cylindrical cross-section shape. It is also observed in Fig. 17 that the peak of the curve tends to occur at the higher pore size when the plate thickness increases. This trend of peak movement representing the correlation of the pore size and the plate thickness gives an idea of the material design. Because the pore size refers to the porogen size, based on Fig. 17, for a given porogen size (or a given plate thickness), we can choose an appropriate plate thickness (or an appropriate porogen size) to obtain the best sound absorbing performance.

7. Conclusion

In this work, we have undertaken essential numerical characterizations of effective mechanical, hydraulic and acoustic properties of a new kind of bio-sourced porous epoxy resin. This novel material has been the product of an environmentally friendly process combining delicately the cationic photopolymerization and the porogen leaching technique. The effective properties of the material have been obtained by conducting an asymptotic homogenization procedure which has lead to macroscopic constitutive and governing equations of an anisotropic poroelastic medium which were first given by Biot. Different from Biot's theory, which deals with a phenomenological approach of the macroscopic behaviour of the poroelastic material, and as a consequence, there is no connection with the microstructure, the applied homogenization method has started from equations at the microscopic scale and has allowed a parametric investigation of the influences of material microstructures on the macroscopic properties.

In this study, homogenization calculations have been performed on representative volume elements which have been based on the idealized fillet-edge cubic elementary pore and matrix obtained from the experimental pore characterization of the material. Following the determination of effective properties by the homogenization method, a normal incidence sound absorption problem has been considered with the use of a plate made of the elaborated material as a porous absorber. After validated by a good match between numerical acoustic

properties and experimental ones resulting from the three-microphone impedance tube testing, the sophisticated framework has been utilized to carry out a parametric study of the effect of the pore arrangements, the porosity and the pore size on the effective properties and acoustic performance of the material.

Based on the results of the parametric investigations, suggestions have been made for the attainment of porous epoxy resins with good sound absorption. Regarding pore arrangements, the results have indicated that if porogen particles could be ordered to make the template, the arrangements 2, 3 and 4 should be chosen rather than the arrangement 1 to obtain a material with better sound absorption. Related to influences of the porosity, the paper has suggested that for better sound absorption at very low frequencies, the material would need to have more porosity which could be attained by raising the pressure and the temperature during the SPS process of the porogen template, whereas at higher frequencies, the less-porosity material obtained from the decrease in the pressure and the temperature during the SPS process without loosing the pore interconnection should be used. It is worth reminding that improving the sound absorption at lower frequencies by increasing the porosity leads to the material with lower stiffness. Therefore, for a specific application of the material such as in civil engineering, there needs a compromise between the mechanical and acoustic properties of the material. Conversely, when a reduction in pressure and temperature is applied to obtain a less-porous and accordingly better sound absorbing material at higher frequencies, both of these two processing parameters should not be decreased too much to avoid the loss of contacts among porogen particles, assuring the availability of sintered porogen templates. Concerning pore size's effects, the obtained pore size *versus* SAA relationships corresponding to different plate thicknesses can play the role of a practical guide for material elaboration processing because the pore size also refers to the porogen size. From these curves, for a given porogen size (or a given plate thickness), we can choose an appropriate plate thickness (or an appropriate porogen size) to obtain the material with the best sound absorbing performance.

Regarding the experimental aspect, additional systematic experiments are needed to identify the lowest porosity and the corresponding critical values of pressure and temperature for ensuring the attainment of sintered templates and hence porous materials. This effort will help to frame the possible range of porosity of porous materials that result from the application of the salt leaching technique. Furthermore, in order to favour the wideband sound absorption of the materials for more potential applications, another attention is paid to the development of multiple-porosity materials such as doubly porous ones [43]. Within the context of the porogen leaching technique, besides macropores obtained by using salt particles as macro-porogens, micropores can be generated by the introduction of porogenic solvents to the formulation [2]. However, because the porogen leaching technique is employed in conjunction with the cationic photopolymerization which is solvent-sensitive, the choice of solvents that are a little harmful and compatible with the cationic photopolymerization would be an interesting challenge.

Concerning the numerical part, the multiscale approach employed in this work concerning the use of ordered microstructures has proved to be useful in the material development stage for obtaining a first estimate of the main physical properties of the real samples as

well as for systematic investigations into the relations between microstructures and effective properties of the studied material, providing valuable suggestions for the material improvement. Nonetheless, it is likely that deeper insights into the effective material's properties could be obtained by including a certain degree of randomness in the orientation and distribution of the pores [44], which will be the topic of a further study. Additionally, for the case of doubly porous materials as above-mentioned, an adapted three-scale asymptotic homogenization procedure would be of interest to deal with the simultaneous presence of macropores and micropores resulting from the use of solid macro-porogens and porogenic solvents, respectively, which exhibit two distinct populations in terms of pore size, pore shape, pore arrangement and porosity.

Data availability

The processed data required to reproduce these findings cannot be shared at this time as the data also forms part of an ongoing study.

Acknowledgements

This work has benefited from a French government grant managed by ANR within the frame of the national program of Investments for the Future ANR-11-LABX-0022-01 (LabEx MMCD project).

References

[1] Q.-B. Nguyen, N.-H. Nguyen, A. Rios de Anda, V.-H. Nguyen, D.-L. Versace, V. Langlois, S. Naili, E. Renard, Photocurable bulk epoxy resins based on resorcinol derivative through cationic polymerization, Journal of Applied Polymer Science (2020) e49051.

[2] H.-B. Ly, B. Le Droumaguet, V. Monchiet, D. Grande, Designing and modeling doubly porous polymeric materials, The European Physical Journal Special Topics 224 (9) (2015) 1689–1706.

[3] Y. Nam, T. Park, Biodegradable polymeric microcellular foams by modifed thermally induced phase separation method, Biomaterials 20 (1999) 1783–1790.

[4] M. Silverstein, N. Cameron, PolyHIPEs - Porous polymers from high internal phase emulsions, in: John Wiley & Sons, Inc. (Ed.), Encyclopedia of Polymer Science and Technology, John Wiley & Sons, Inc., Hoboken, NJ, USA, 2010.

[5] Q. Qi, P. Zheng, Y. Lei, X. Liu, Design of bi-modal pore structure polyarylene ether nitrile/sio2 foams with ultralow-k dielectric and wave transparent properties by supercritical carbon dioxide, Composites Part B: Engineering 173 (2019) 106915.

[6] G. Chen, T. Ushida, T. Tateishi, Preparation of poly(l-lactic acid) and poly(dl-lactic-co-glycolic acid) foams by use of ice microparticulates, Biomaterials 22 (18) (2001) 2563–2567.

[7] K. Rezwan, Q. Chen, J. Blaker, A. Boccaccini, Biodegradable and bioactive porous polymer/inorganic composite scaffolds for bone tissue engineering, Biomaterials 27 (18) (2006) 3413–3431.

[8] Q. Tann, S. Li, J. Ren, C. Chen, Fabrication of porous scaffolds with a controllable microstructure and mechanical properties by porogen fusion technique, International Journal of Molecular Sciences 12 (2) (2011) 890–904.

[9] J. L. Auriault, C. Boutin, C. Geindreau, Homogenization of Coupled Phenomena in Heterogenous Media, Wiley-ISTE, 2009.

[10] A. Mielke, E. Rohan, Homogenization of elastic waves in fluid-saturated porous media using the biot model, Mathematical Models and Methods in Applied Sciences 23 (5) (2013) 873–916.

[11] R. Del Toro, A. Bacigalupo, M. Paggi, Characterization of wave propagation in periodic viscoelastic materials *via* asymptotic-variational homogenization, International Journal of Solids and Structures 172-173 (2019) 110–146.
[12] M. De Bellis, A. Bacigalupo, G. Zavarise, Characterization of hybrid piezoelectric nanogenerators through asymptotic homogenization, Comput. Methods Appl. Mech. Engrg. 355 (2019) 1148–1186.
[13] L. Maheo, P. Viot, D. Bernard, A. Chirazi, G. Ceglia, V. Schmitt, O. Mondain-Monval, Elastic behavior of multi-scale, open-cell foams, Composites Part B: Engineering 44 (1) (2013) 172–183.
[14] F. Chevillotte, C. Perrot, Effect of the three-dimensional microstructure on the sound absorption of foams: A parametric study, The Journal of the Acoustical Society of America 142 (2) (2017) 1130–1140.
[15] A. Azarniya, A. Azarniya, M. Safavi, M. Ahmadipour, M. Seraji, S. Sovizi, M. Saqaei, R. Yamanoglu, M. Soltaninejad, H. Hosseini, S. Ramakrishna, A. Kawasaki, S. Adams, M. Reddy, Physicomechanical properties of porous materials by Spark Plasma Sintering, Critical Reviews in Solid State and Materials Sciences (2019) 1–44.
[16] H. Giesche, Mercury porosimetry: A general (practical) overview, Particle & Particle Systems Characterization 23 (1) (2006) 9–19.
[17] E. Rohan, S. Naili, R. Cimrman, T. Lemaire, Multiscale modeling of a fluid saturated medium with double porosity: Relevance to the compact bone, Journal of the Mechanics and Physics of Solids 60 (5) (2012) 857 – 881.
[18] T. Yamamoto, S. Maruyama, K. Terada, K. Izui, S. Nishiwaki, A generalized macroscopic model for sound-absorbing poroelastic media using the homogenization method, Computer Methods in Applied Mechanics and Engineering 200 (1-4) (2011) 251–264.
[19] E. Sanchez-Palencia, Non-Homogeneous Media and Vibration Theory, no. 127 in Lecture Notes in Physics, Springer, Berlin, 1980.
[20] J.-L. Auriault, L. Borne, R. Chambon, Dynamics of porous saturated media, checking of the generalized law of Darcy, The Journal of the Acoustical Society of America 77 (5) (1985) 1641–1650.
[21] V.-H. Nguyen, E. Rohan, S. Naili, Multiscale simulation of acoustic waves in homogenized heterogeneous porous media with low and high permeability contrasts, International Journal of Engineering Science 101 (2016) 92–109.
[22] J.-F. Allard, N. Atalla, Propagation of Sound in Porous Media: Modelling Sound Absorbing Materials, 2nd Edition, Wiley, 2009.
[23] R. Panneton, X. Olny, Acoustical determination of the parameters governing viscous dissipation in porous media, The Journal of the Acoustical Society of America 119 (4) (2006) 2027–2040.
[24] X. Olny, R. Panneton, Acoustical determination of the parameters governing thermal dissipation in porous media, The Journal of the Acoustical Society of America 123 (2) (2008) 814–824.
[25] COMSOL Multiphysics, COMSOL AB, Stockholm, Sweden (2019).
[26] K. Gross, L. Rodrıǵuez-Lorenzo, Biodegradable composite scaffolds with an interconnected spherical network for bone tissue engineering, Biomaterials 25 (20) (2004) 4955–4962.
[27] V.-H. Nguyen, S. Naili, Semi-analytical solution of transient plane waves transmitted through a transversely isotropic poroelastic plate immersed in fluid, Journal of Engineering Mathematics 86 (1) (2014) 125–138. doi:10.1007/s10665-013-9654-5.
[28] N. Gorbushin, S. Naili, V.-H. Nguyen, Optimizing microstructure of a poroelastic layer with cylindrical pores for absorption properties, Mechanics Research Communications 102 (2019) 103422.
[29] N. Gorbushin, V.-H. Nguyen, S. Naili, Design optimisation of acoustic absorbers with cross-like pores *via* a homogenisation method, Acta Acustica united with Acustica 105 (2019) 638–649.
[30] H. Kuttruff, Acoustics: An Introduction, Taylor & Francis, 2007.
[31] C. Perrot, F. Chevillotte, R. Panneton, Bottom-up approach for microstructure optimization of sound absorbing materials, The Journal of the Acoustical Society of America 124 (2) (2008) 940–948.
[32] Y. Salissou, R. Panneton, Wideband characterization of the complex wave number and characteristic impedance of sound absorbers, The Journal of the Acoustical Society of America 128 (5) (2010) 2868–2876.
[33] D. Johnson, J. Koplik, L. Schwartz, New pore-size parameter characterizing transport in porous media,

Phys. Rev. Lett. 576 (1986) 2564–2567.
[34] D. L. Johnson, J. Koplik, R. Dashen, Theory of dynamic permeability and tortuosity in fluid-saturated porous media, Journal of Fluid Mechanics 176 (1987) 379.
[35] Y. Champoux, J.-F. Allard, Dynamic tortuosity and bulk modulus in air-saturated porous media, Journal of Applied Physics 70 (4) (1991) 1975–1979.
[36] D. Lafarge, P. Lemarinier, J. F. Allard, V. Tarnow, Dynamic compressibility of air in porous structures at audible frequencies, The Journal of the Acoustical Society of America 102 (4) (1997) 1995–2006.
[37] X. Luo, P. Were, J. Liu, Z. Hou, Estimation of Biot's effective stress coefficient from well logs, Environmental Earth Sciences 73 (11) (2015) 7019–7028.
[38] R. Baker, H. Yarranton, J. Jensen, Practical Reservoir Engineering and Characterization, Elsevier, 2015.
[39] L. Zhang, Y. Zhang, Y. Jiang, R. Zhou, Mechanical behaviors of porous Ti with high porosity and large pore size prepared by one-step spark plasma sintering technique, Vacuum 122 (2015) 187–194.
[40] ASTM International, Standard test method for sound absorption and sound absorption coefficients by the reverberation room method, American Society for Testing and Materials (2002).
[41] M. Zainulabidin, M. Rani, N. Nezere, A. Tobi, Optimum sound absorption by materials fraction combination, International Journal of Mechanical & Mechatronics Engineering 14 (02) (2014) 4.
[42] G. Kirchhoff, On the influence of heat conduction in a gas on sound propagation, R.B. Lindsay, Ed., Physical Acoustics (1974) 7–19.
[43] E. Rohan, V.-H. Nguyen, S. Naili, Numerical modelling of waves in double-porosity Biot medium, Computers and Structures 232 (2020) 105849.
[44] C. Nguyen, J. Guilleminot, F. Detrez, V. Langlois, M. Bornert, A. Duval, C. Perrot, Micro-macro acoustic modeling of heterogeneous foams with nucleation perturbation, in: 11th International Styrian Noise, Vibration & Harshness Congress: The European Automotive Noise Conference, SAE International, 2020.